Ruthenium supported on silicate and aluminosilicate mesoporous materials applied to selective sugar hydrogenation: Xylose to xylitol

Araujo-Barahona, German; Shcherban, Nataliya; Eränen, Kari; Kopa, Ivan; Bezverkhyy, Igor; Martínez-Klimov, Mark; Vajglová, Zuzana; Aho, Atte; García-Serna, Juan; Salmi, Tapio; Murzin, Dmitry Yu

Published in:
Chemical Engineering Journal

DOI:
10.1016/j.cej.2024.150019

Published: 01/04/2024

Document Version
Final published version

Document License
CC BY

Chemical Engineering Journal 485 (2024) 150019

Contents lists available at ScienceDirect

Chemical Engineering Journal

journal homepage: www.elsevier.com/locate/cej

Ruthenium supported on silicate and aluminosilicate mesoporous materials applied to selective sugar hydrogenation: Xylose to xylitol

German Araujo-Barahona [a,b], Nataliya Shcherban [c], Kari Eränen [a], Ivan Kopa [c], Igor Bezverkhyy [d], Mark Martínez-Klimov [a], Zuzana Vajglová [a], Atte Aho [a], Juan García-Serna [b], Tapio Salmi [a], Dmitry Yu. Murzin [a,*]

[a] Laboratory of Industrial Chemistry and Reaction Engineering (TKR), Johan Gadolin Process Chemistry Centre (PCC), Åbo Akademi University, FI-20500 Turku, Åbo Finland

[b] Grupo de Tecnologías a Presión (PressTech), Instituto de Bioeconomía de la Universidad de Valladolid (BioEcoUVa), Departamento de Ingeniería Química y Tecnología del Medio Ambiente, Escuela de Ingenierías Industriales, Universidad de Valladolid, ES-47011 Valladolid, Spain

[c] Department of Porous Substances and Materials, L.V. Pisarzhevsky Institute of Physical Chemistry, National Academy of Sciences of Ukraine, 31 pr. Nauky, UA-03028 Kyiv, Ukraine

[d] Laboratoire Interdisciplinaire Carnot de Bourgogne, UMR 6303 CNRS-Université de Bourgogne-Franche Comté, 9 Av. A. Savary, BP 47870, FR-21078 Dijon Cedex, France

ARTICLE INFO

Keywords:
Biorefinery
Mesoporous molecular sieves
MCM-41
Sugar alcohols
Ruthenium
Hydrogenation

ABSTRACT

A series of ruthenium-based catalysts supported on a set of silicate and aluminosilicate mesoporous molecular sieves was synthesized and tested in xylose hydrogenation. The materials were characterized in terms of morphology, textural properties, acidity, as well as ruthenium loading, dispersion, and oxidation state. In general, the aluminosilicates-based catalysts displayed a higher activity compared to their respective silicate supports, which can be ascribed to a higher Ru content and dispersion, enhanced by a higher acidity. The most active synthesized catalyst (Ru/Al-MCM-4) displayed an improved performance compared to a commercial Ru/C catalyst due to a better xylitol selectivity. Two modelling approaches were implemented to describe the kinetic rate. The first model was based on the hypothesis that xylose molecules and hydrogen are adsorbed in different active sites on the catalyst surface, while the second model supposes the formation of an intermediate on the catalyst surface that reacts to form xylitol. Both models gave a very good description of the experimental data.

1. Introduction

Production of sugar alcohols exemplifies an industrially relevant application of the second-generation biorefinery concept [1] as the sugars used for this process are obtained through the extraction and processing of hemicelluloses. Hemicelluloses are found in biomass materials such as softwood and hardwood, pulp liquors from the pulp and paper industry, as well as agricultural residues [2]. Sugar alcohols are polyols formed through the reduction of the carbonyl group in sugar molecules. This reduction process can be achieved using chemical reagents, such as sodium borohydride, or molecular hydrogen in the presence of either a homogeneous or heterogeneous catalyst [3–5]. The route based on the use of heterogenous catalysts is preferred from an environmental point of view since it avoids formation of stoichiometric co-products and facilitates the separation processes [4,6]. In the recent years, alternative production routes have been explored, particularly through a biotechnological approach utilizing microorganisms such as the enzyme NAD(P)H-dependent xylose reductase. While this method presents an advantage of milder conditions compared to traditional chemical routes, the feasibility for large-scale production is hindered by the low yields [7].

Xylitol is one of the most produced sugar alcohols worldwide due to its wide range of applications [7,8]. This polyol is used as a low-calorie sweetener in the alimentary industry and as an anti-caries agent and excipient in pharmaceutical products [9].

Industrial xylitol production involves extraction of xylan (a hemicellulose), followed by acid hydrolysis and purification to yield the xylose monomer. Subsequently, xylose undergoes hydrogenation in the presence of a finely dispersed Ni-based catalyst, primarily using Raney nickel. The hydrogenation reaction is conducted in pressurized semi-

* Corresponding author.
E-mail address: dmurzin@abo.fi (D.Yu. Murzin).

https://doi.org/10.1016/j.cej.2024.150019
Received 27 November 2023; Received in revised form 31 January 2024; Accepted 25 February 2024
Available online 27 February 2024

batch reactors, maintaining a constant temperature (120–150 °C) and hydrogen pressure (30–70 bar). Solid xylitol with a purity of 99 % is ultimately obtained through a sequential process involving ion exchange chromatography followed by crystallization [10]. However, the pyrophoric nature and susceptibility to metal leaching of Raney nickel have adverse effects on its handling and durability. Consequently, ruthenium catalysts are expected to make a breakthrough [6] in sugar alcohol production due to the ability of this noble metal to selectively hydrogenate carbonyl group compounds in aqueous media [11,12].

Ruthenium has been demonstrated as an efficient hydrogen-transfer catalyst in a variety of relevant biomass upgrading reactions, such as levulinic acid hydrogenation to γ-valerolactone (GVL) [13], furfural hydrogenation [14] to a variety of different products, particularly 2-methylfural [15], as well as for the hydrogenation of bicyclic heteroaromatic compounds (quinolines, indoles, benzopyrans, and benzofurans) to obtain compounds with antioxidant, anti-inflammatory, and cytotoxic properties, which are attractive for several specialized applications [16].

Specifically on sugar hydrogenation, the effectiveness of Ru has been demonstrated by extensive experimental evidence [17–19] and theoretical considerations [20]. Among the conventional metals used for sugar hydrogenation, Ru exhibits the highest catalytic activity (Ru > Ni > Rh > Pd) [21] along with a good stability under optimal reaction conditions [22]. Thus, in recent years, several studies have focused on the development of suitable supported Ru catalysts [19,23–25]. The selected support should have adequate interactions with the Ru nanoparticles deposited on the support, allowing a good distribution and stability of the active phase to minimize metal leaching and nanoparticle sintering. Moreover, the textural properties of the support, such as surface area and pore size distribution, should ensure the accessibility of relatively large sugar molecules from the liquid phase to the Ru nanoparticles. In this sense, mesoporous molecular sieves (MCF, MCM-41, and SBA-15) might be interesting catalyst supports for ruthenium applied to sugar alcohol production.

Molecular sieves offer interesting properties such as highly ordered structure and developed porosity, as well as a high surface area and tunable acid-base properties to enhance the interactions with Ru precursor solutions. The feasibility of using Ru-based catalyst has been demonstrated by Romero et al. using a Ru/MCM-48 catalyst for one-pot conversion of cellulose to sorbitol [26]. Zhang et al. utilized a Ru/MCM-41 catalyst for sorbitol production from glucose and reported a performance similar to a commercial Ru/C catalyst, while Melero et al. screened ruthenium catalysts supported on ZrO_2-SBA-15 for glucose hydrogenation [27]. High sorbitol selectivity was achieved along with improved stability, as superior active metal-support interactions prevented agglomeration of Ru nanoparticles.

The objective of this work was to develop Ru catalysts supported on different silicate and aluminosilicate mesoporous materials (Ru/Al-MCM-41, Ru/Al-MCF, Ru/Al-Si-SBA-15, Ru/Si-SBA-15, and Ru/Si-MCM-41) and to evaluate their catalytic activity for xylose hydrogenation to xylitol. A series of characterization techniques was applied to elucidate the impact of the materials properties with catalytic activity. The synthesized materials were characterized in terms of morphology, textural properties, acidity, ruthenium loading, dispersion, and oxidation state, and their activities were compared with a commercial Ru/C catalyst. The effect of temperature and pressure on xylose hydrogenation was studied for Ru/Al-MCM-41 through experiments in a semi-batch laboratory-scale reactor. Finally, two kinetic models were developed featuring between non-competitive adsorption of reactants and formation of a dihydrogen-containing intermediate on the catalyst surface that is isomerized to the product on the surface.

2. Experimental part

2.1. Materials and reagents

Cetyltrimethylammonium chloride (CTACl, 25 wt% solution in water), tetraethyl orthosilicate (TEOS, ≥99.0 %), aluminum isopropoxide (≥98.0 %), Pluronic P-123 [$HO(CH_2CH_2O)_{20}(CH_2CH(CH_3)O)_{70}(CH_2CH_2O)_{20}H$], 1,3,5-trimethylbenzene (TMB, 98.0 %), ammonium fluoride (≥98.0 %), ruthenium(III) chloride hydrate (Merck, ReagentPlus®), hydrochloric acid (35 wt%) was purchased from VWR, ammonium hydroxide solution (25 wt%) was purchased from Supelco, sulfuric acid 96 wt%, nitric acid 65 wt%, D-xylose (≥99.0 %), xylitol (≥99.0 %), D-arabitol (99.0 %) and *meso*-erythritol were purchased from Sigma-Aldrich. A commercial sample of Ru/C (6 wt% Ru) catalyst was used for benchmarking.

2.2. Catalysts preparation

MCF, MCM and SBA type mesoporous molecular sieves (MMS) in the form of silica and aluminosilicate materials were applied as supports for the Ru deposition.

2.2.1. Si-MCM-41 synthesis

This material was obtained according to the conventional method with some modifications [28,29]. The composition of the reaction mixture was $1.0SiO_2$:0.5CTACl:$8NH_4OH$:$76H_2O$. 56.8 mL of ammonia solution was slowly added to 32.4 mL of CTACl solution under stirring. The resulting mixture was stirred for 30 min and 10.8 mL of TEOS was added followed by stirring the resulting RM for another 90 min. Thereafter, the obtained mixture was subjected to hydrothermal treatment at 100 °C for 72 h.

2.2.2. Al-MCM-41 synthesis

Al-containing MCM-41 material was synthesized according to the method similar to aforementioned Si-MCM-41 synthesis technique using aluminum isopropoxide as a source of aluminum. The composition of the reaction mixture (Si/Al = 50) was: $1.0SiO_2$:$0.01Al_2O_3$:0.5CTACl:$8NH_4OH$:$76H_2O$. 56.8 mL of ammonia solution was slowly added to 32.4 mL of CTACl solution (25 wt%) under stirring. The resulting mixture was stirred for 30 min and 0.202 g of aluminum isopropoxide was added. After 10 min of stirring, 10.8 mL of TEOS was added and the reaction mixture was continued stirring for another 90 min. Thereafter, the obtained reaction mixture was subjected to hydrothermal treatment at 100 °C for 72 h.

2.2.3. Si-SBA-15 synthesis

The synthesis of Si-SBA-15 was carried out according to the method described in Ref. [30] with some modification. The composition of the RM was: 1.0SiO2:0.016Pluronic P-123:5.5HCl:152H2O. 0.8 g of Pluronic P-123 was dissolved in 24 mL of water and 4 mL of HCl (35 %) at 40 °C for 24 h under stirring. 2 mL of TEOS was added to the resulting solution, and the RM was stirred at a temperature of 40 °C for 20 h. The resulting mixture (pH = 0.35) was subjected to hydrothermal treatment at 100 °C for 24 h.

2.2.4. Al-SBA-15 synthesis

The synthesis of AlSi-SBA-15 was carried out using a method described in Ref. [31] with some modifications. The composition of the reaction mixture (Si/Al = 50) was $1.0SiO_2$:$0.01Al_2O_3$:0.016Pluronic P-123:5.5HCl:$152H_2O$. 2.12 g of Pluronic P-123 was dissolved in 64 mL of water and 10.6 mL of HCl (35 %) at 40 °C for 24 h under stirring. Then, 0.048 g of aluminum isopropoxide was added to the resulting solution and the mixture was stirred for 15 min at the same temperature. Thereafter, 5.2 mL of TEOS was added to the solution, and the reaction mixture was stirred at 40 °C for 20 h. The resulting mixture was exposed to hydrothermal treatment at a temperature of 100 °C for 24 h. For the incorporation of aluminum into SBA-15, the pH of the resulting gel (pH = 0.35) was corrected to 7.5 by adding an ammonia solution (25 %). Then, the hydrothermal treatment was repeated at the same temperature and for the same duration.

2.2.5. Al-MCF synthesis

The Al-containing MCF material was synthesized according to the method described in Ref. [32] with some modifications. The composition of the RM (Si/Al = 50) was $1.0SiO_2$:$0.01Al_2O_3$:0.009Pluronic P-123:0.41TMB:0.015NH_4F:1.3HCl:50·.5H_2O 3.03 g of Pluronic P-123 was dissolved in 49 mL of water and 7.1 mL of HCl (35 %) at 40 °C for 24 h under stirring. Then, 3.5 mL of TMB was added and the mixture was stirred for 2 h. Thereafter, 0.249 g of aluminum isopropoxide was added to the resulting solution and the mixture was stirred for 15 min at the same temperature. Then, 13.7 mL of TEOS was added to the solution, and the reaction mixture was stirred at 40 °C for 20 h. 0.035 g of NH_4F was added into the resulting mixture, and the mixture was subjected to hydrothermal treatment at a temperature of 100 °C for 24 h. For incorporation of aluminum into the MCF material, the pH of the resulting gel (pH = 0.35) was adjusted to 7.5 by adding an ammonia solution (25 wt%). Then, the hydrothermal treatment was repeated at the same temperature and duration.

The obtained products were isolated by filtration, washed with distilled water to neutral pH and absence of the surfactant release in the filtrate. Subsequently, the powders were dried at 100 °C overnight and calcined at 550 °C for 5 h with a heating rate of 2 °C•min^{-1}.

2.2.6. Deposition of Ru nanoparticles onto mesoporous molecular sieves

MMS supported Ru nanoparticles were prepared using wet impregnation followed by reduction with hydrogen. For all catalysts, the nominal loading of Ru was 2 wt%. Prior to impregnation, MMS were activated at 450 °C for 5 h with a heating rate of 2 °C•min^{-1}. In a typical procedure, 2.93 mL of 0.2 M $RuCl_3$ solution and 2.9 g of MMS was added to 2.4 L of H_2O and the suspension was stirred at a room temperature for 15 h. Then, the suspension was rotary evaporated at 60 °C and the obtained solid was dried at 60 °C for 24 h and at 120 °C for 3 h. The obtained material was reduced with hydrogen for 3 h at 350 °C with a temperature ramp of 5 °C•min^{-1}.

2.3. Catalyst characterization

X-ray diffractometer D8 ADVANCE (Bruker AXS) with CuKα-radiation was used for the analysis of the phase composition of the obtained samples.

SEM images of the samples were obtained using field emission SEM JSM-7600F (JEOL). The images were recorded using the accelerating voltage of 1 – 30 kV and a secondary electron detector. A sample was loaded on the conductive graphitized support and the recording was carried out without any preliminary deposition of conductive materials on the sample surface.

The size distributions of the Ru nanoparticles on the tested materials were determined using transmission electron microscopy (TEM, JEM 1400 Plus Transmission Electron Microscope). Approximately 500 particles were measured per each sample in Image J software. The metal dispersion (D) was determined using eq. (1), where d_{Ru} is the mean nanoparticle size, while v_m and a_m are the volume and area occupied by a Ru atom, respectively. A hexagonal closed pack (hcp) structure was assumed with values of $a_m = 0.064$ nm^2 and $v_m = 0.0137$ nm^3 [33].

$$D = 6 \cdot \frac{v_m}{a_m} \cdot \frac{1}{d_{Ru}} \quad (1)$$

The initial turnover frequency of xylose hydrogenation for every catalyst was calculated using eq. (2), where r_0 is the initial reaction rate per mass of ruthenium and M_{Ru} is the molar mass of ruthenium.

$$TOF_0 = \frac{r_0 \cdot M_{Ru}}{D} \quad (2)$$

The ruthenium content of the catalysts as well as the degree of ruthenium leaching during the experiments were determined through Inductively Coupled Plasma Optical Emission Spectroscopy (ICP-OES) (PerkinElmer, Optima 5300 DV). Prior to the analysis, the catalysts were dissolved in a microwave oven using a mixture of acids (3 mL of sulfuric acid + 3 mL of nitric acid). The degree of leaching in the reaction mixture was determined by comparing the Ru concentration before and after 4 h of the kinetic experiment at different temperatures.

The molar ratio of Si/Al in the samples was determined using X-ray fluorescence spectrometer (ElvaxPlus).

Nitrogen physisorption was utilized to estimate the surface area, pore volume and pore size distribution of the tested catalysts (Micromeritics 3Flex-3500). The samples were outgassed for 24 h at 200 °C prior to analysis. The specific surface area S_{BET} was evaluated using BETSI algorithm [34]; the micropore and mesopore size distribution curves were obtained by the NLDFT method [35] using the desorption branch of the isotherm. The micropore volume (V_{micro}), the mesopore volume (V_{meso}) and the mesopore surface area (S_{meso}) were determined by the comparative t-plot method [36–38].

The pyridine (Py) adsorption with FTIR-spectral analysis was used to characterize the type, strength, and concentration of acid sites in the catalysts. The thin plates of the studied samples (without a binder) were placed in a cuvette with NaCl windows and evacuated (P = 1.4 Pa) at 450 °C for 1 h; pyridine was adsorbed at 150 °C (in a cuvette with a sample) for 15 min, and desorbed at 150 – 450 °C with a 100 °C interval and a holding time of 30 min. Spectra of adsorbed pyridine were recorded using a Fourier spectrometer Spectrum One (Perkin Elmer). The concentration of Lewis (LAS) and Brønsted (BAS) acid sites were determined from the integral intensity of the absorption bands at 1454 cm^{-1} and 1545 cm^{-1} respectively using the integral molar absorption coefficients for these bands: ε(LAS) = 2.22 cm/μmol and ε(BAS) = 1.67 cm/μmol reported for AlSBA-15 [39,40] and amorphous silica-alumina [41].

Temperature-programmed reduction (TPR) was performed using Microtrac Belcat II to determine the reduction temperature and hydrogen consumption of the fresh catalysts. For an experiment, about 30 mg of the catalyst was loaded into a quartz reactor and pretreated *in-situ* at 400 °C for 2 h under argon flow to remove excess moisture. The analysis was carried out under a 5 % H_2/Ar flow in the temperature range from 35 °C to 800 °C with a temperature ramp of 10 °C/min.

X-ray photoelectron spectroscopy (XPS) was utilized to investigate the oxidation state of Ru on the two screened catalysts with the superior performance for xylose hydrogenation (Ru/C and Ru/Al-MCM-41). The catalysts were analyzed as fresh ones and after being used for xylose hydrogenation (90 °C and 40 bar of hydrogen pressure). The XPS measurements were performed in a Thermo Scientific Nexsa G2 X-Ray Photoelectron Spectrometer using a monochromated Al Kα excitation source. The pressure in the XPS analysis chamber was less than $2x10^{-9}$ mbar. The carbon peak C 1 s at 284.8 eV was used as binding energy reference. The analysis of the spectra was carried out in the Ru 3d region. The components were assigned in accordance with previously reported data as Ru^0 at 279.75 ± 0.37 eV, RuO_2 (Ru^{+4}) at 281.37 ± 1.32 eV, and $RuCl_3$ (Ru^{+3}) at 282.4 ± 0.45 eV [42], and a hypothetical RuO_x (Ru^{+x}) compound. Additional peaks corresponding to carbonaceous compounds present on the catalyst surface were included too. The background shape of the spectrum was fitted with the Shirley algorithm, and the elemental chemical states of Ru were fitted with a combined Gaussian-Lorentzian curves with a G:L ratio of 70:30. Symmetric peaks with a doublet separation of 4.15 eV were used to fill the Ru $d_{5/2}$ region, following the methodology implemented by Balcerzak et al. [43].

2.4 Kinetic experiments

Kinetic experiments were carried out in a laboratory-scale semi batch reactor (Parr 4843, 300 mL) equipped with a pre-heating chamber, a heating jacket for the reactor vessel, and a sampling line with a 7 μm filter. Before each experiment the system was purged with argon and hydrogen, followed by reduction of the catalyst at 7 bar hydrogen pressure and 120 °C for two hours. The sugar solution was saturated with hydrogen at the corresponding temperature and pressure conditions inside the pre-heating chamber. Thereafter, 130 mL of pre-

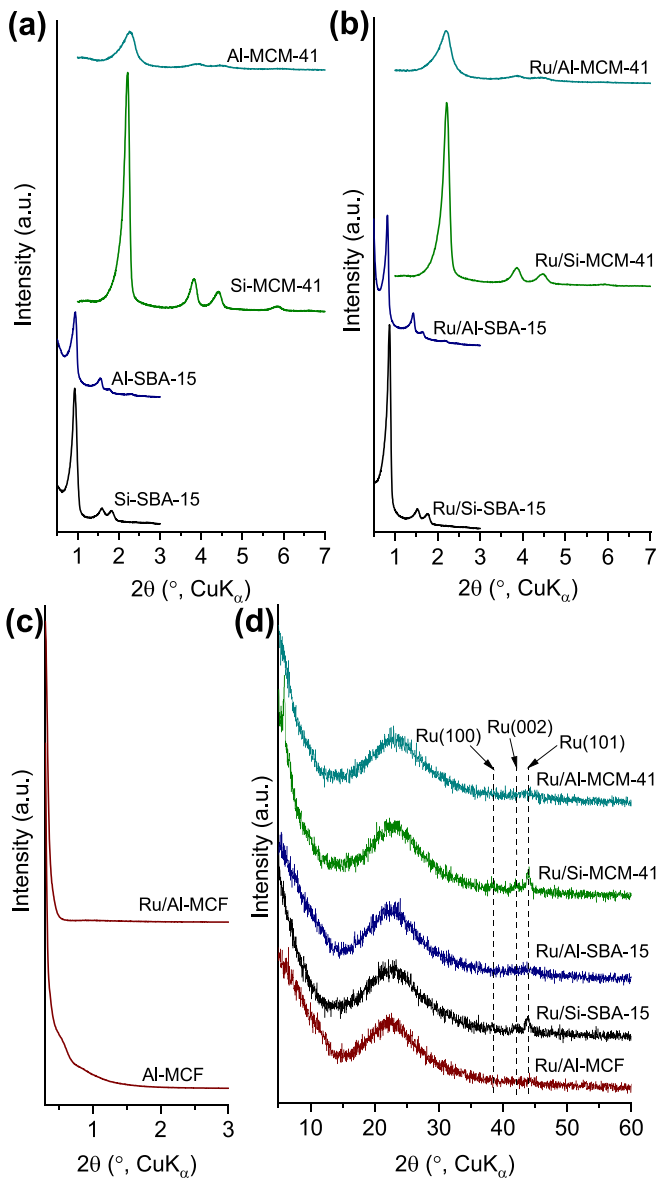

Fig. 1. XRD patterns of the initial supports and prepared supported Ru catalysts in small-angle (a-c) and medium-angle (d) regions.

saturated D-xylose solution with a concentration of 0.13 mol/L was injected into the reactor vessel. A gas entrainment impeller was used at an agitation rate of 1000 rpm to ensure the operation in the absence of external mass transfer limitations. Liquid samples (approximately 0.5 mL per sample) were withdrawn from the reactor at different times.

The concentrations of reactants and products were determined using a Hitachi Chromaster high-performance liquid chromatograph equipped with a refractive index (RI) detector (Hitachi 5450 RI Detector). The mobile phase was a 1.2 mM $CaSO_4$ solution with a volumetric flow 0.3 mL/min. The column temperature was set at 50 °C and the sample injection volume of 10 μL.

The prepared catalysts were tested at 90 °C and 40 bar of hydrogen pressure. A commercial Ru/C catalyst under similar conditions. Moreover, the systematic kinetic study with the most active catalyst (Ru/Al-MCM-41) was carried out in a temperature range of 60 – 100 °C and at a hydrogen pressure range of 10 – 50 bar. An experiment was carried out at 90 °C and 40 bar using the recovered catalyst to assess the recyclability of Ru/Al-MCM-41 catalyst. Water from the reaction mixture was removed in a rotatory evaporator at 50 °C. Thereafter, the catalyst was washed in 100 mL of deionized water, then the washing water was decantated and the process was repeated five times. Finally, the recovered catalyst was oven-dried at for 2 h at 110 °C.

3. Experimental results and discussion

3.1 Catalyst characterization results

3.1.1 Structure of the materials, Ru loading and particle size distribution

According to the analysis of the prepared supported samples using X-ray diffraction (Fig. 1), deposition of ruthenium onto the applied MMS did not lead to a decrease in the spatial ordering of the initial supports as XRD patterns in low-angle region retain the corresponding reflexions typical of silica MCM-41, SBA-15, and their aluminosilicate analogues (Fig. 1a, b). Specifically, the indicated supported materials being highly ordered mesostructures, preserved the intensity and resolution of the small-angle reflexes inherent to the initial supports. In case of the MCF support, the corresponding XRD patterns remained similar although a visible low-angle signal was not observed either for the initial Al-MCF, or for the supported Ru sample (Fig. 1c). Considering a weakly expressed low-angle signal in the XRD pattern of the corresponding silica MCF [44], some distortion of the mesocellular structure caused by the incorporation of Al might have appeared. The broad reflexes in the range of 2θ at ca. 20 – 25° (Fig. 1d) originate from the amorphous nature of the initial supports, while deposited Ru particles gave different contributions to the studied catalysts. Specifically, the most intensive Ru reflexes [45] were observed for the Ru catalysts deposited onto silica MCM-41 and SBA-15, while the XRD patterns of the corresponding aluminosilicate-supported materials did not contain signals corresponding to the metal Ru phase, therefore suggesting a high metal dispersion.

According to SEM data, Ru-containing MCM-41, SBA-15 silicates, and SBA-15, MCF aluminosilicates consist of rope-like particles with a size of 1.0 – 1.5 μm (Fig. S1), while MCM-41 aluminosilicate has agglomerated spherical particles with a size of 0.1 – 0.2 μm. The synthesized materials have a Ru loading in the range of 2 – 4 wt%, except for Ru/SiMCM-41, with a loading of 1.2 wt% (Table 1). The lower Ru

Table 1
Ru loading, particle size, dispersion and TOF of the studied materials.

Catalyst	w_{Ru} [a] (wt.%)	d_{Ru} [b] (nm)	D[c]	r_0 (mol•gRu^{-1}•min^{-1}) [d]	TOF_0 (min^{-1})[e]
Ru/Si-MCM-41	1.2	4.8 ± 1.4	0.27	0.029	10.86
Ru/Al-MCM-41	2.9	1.9 ± 1.1	0.68	0.047	6.99
Ru/Si-SBA-15	2.2	3.8 ± 1.3	0.34	0.028	8.32
Ru/Al-SBA-15	3.1	2.3 ± 0.7	0.56	0.039	7.04
Ru/Al-MCF	3.6	2.0 ± 0.9	0.64	0.037	5.84
Ru/C	5.9	4.7 ± 1.5	0.27	0.054	20.21

[a] Ru loading, determined by ICP-OES.
[b] Ru average nanoparticle size from TEM measurements.
[c] Dispersion.
[d] Determined by nonlinear regression as described in the mathematical modelling section.
[e] Initial turnover frequency.

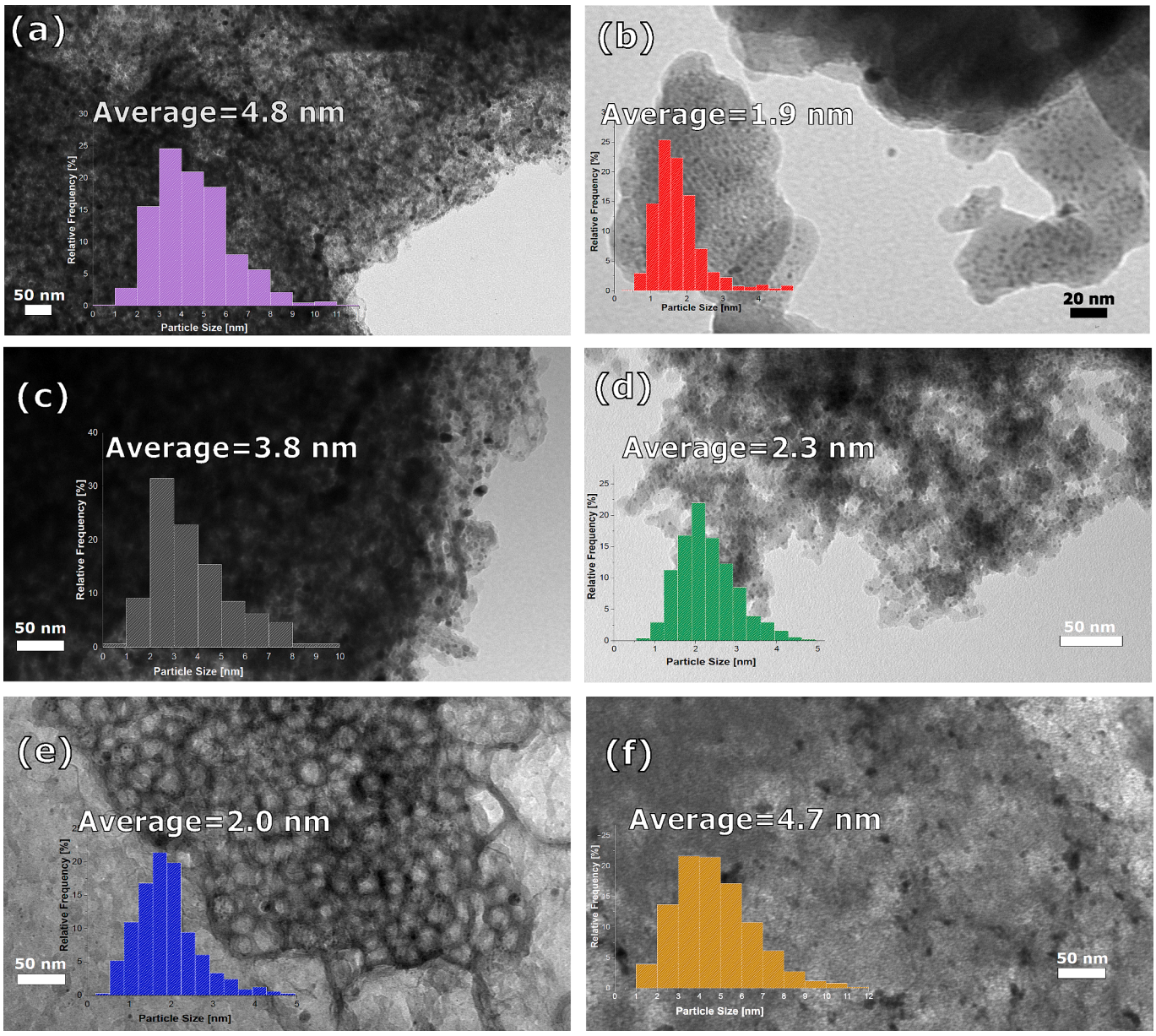

Fig. 2. TEM images of Ru/Si-MCM-41 (a), Ru/Al-MCM-41 (b), Ru/Si-SBA-15 (c), Ru/Al-SBA-15 (d), Ru/Al-MCF (e), Ru/C (f).

loading of the silicate-based materials compared to aluminosilicate-supported samples is obviously associated with a lower metal-support interaction for the Si-based catalysts and its increase in case of the presence of Al species due to the formation of acid sites.

TEM images showed (Fig. 2) an even distribution of Ru nanoparticle in the obtained MMS. Ru/AlSi-SBA-15, Ru/Al-MCM-41, and Ru/Al-MCF catalysts exhibit the lowest Ru mean nanoparticle size (ca. 2 nm, Table 1, Fig. 2) and the highest metal dispersion (ca. 50 %) among the synthesized materials and a similar catalytic activity as discussed in Section 3.2.1. Ru/Si-MCM-41, Ru/Si-SBA-15, and Ru/C possess significantly larger Ru nanoparticles (4 – 5 nm) and lower metal dispersion (ca. 20 %).

3.1.2 Textural properties

Fig. 3 displays the nitrogen physisorption isotherms and the pore size distribution of the catalysts, with their textural properties collected in Table 2. The Ru/Si-MCM-41 and Ru/Al-MCM-41 catalysts display an isotherm type IV with an inflection point located around the relative pressure value of 0.3 and slight hysteresis loop. These features are typical of the materials with a regular mesoporous structure such as MCM-41 [1]. Ru/Si-SBA-15, Ru/Al-SBA-15, and Ru/Al-MCF have an isotherm IV with inflection points close to the relative pressure of 0.6 – 0.8 and well-pronounced hysteresis loops of type H2(a), observed frequently in mesoporous ordered silica materials after hydrothermal treatment and in mesocellular silica foams [46]. Ru/C displays an isotherm type I, typical for microporous materials such as activated carbons [46]. The porous structure of this material also contains slitlike mesopores (H4 loop at $p/p_0 > 0.4$ in isotherm). The pore size distribution (Fig. 3b) also reveals that the synthesized materials have mainly mesoporous nature (3.8 – 31.1 nm), while the commercial carbon-based catalyst have both micropores (0.59 nm) and mesopores with a broad size distribution. The micropores of Ru/Si-SBA-15, Ru/Al-SBA-15, and Ru/Al-MCF are originated from the removal of the hydrophilic polyethylene oxide units of Pluronic P-123 contained in the wall of the as-synthesized MMS. Ru/Si-MCM-41 and Ru/Al-MCM-41 have relatively narrow mesopores (ca. 4 nm, Table 2) and well-developed mesopore surface (S_{meso} = 595 – 640 m^2/g). Ru/Si-SBA-15, Ru/Al-SBA-15, and

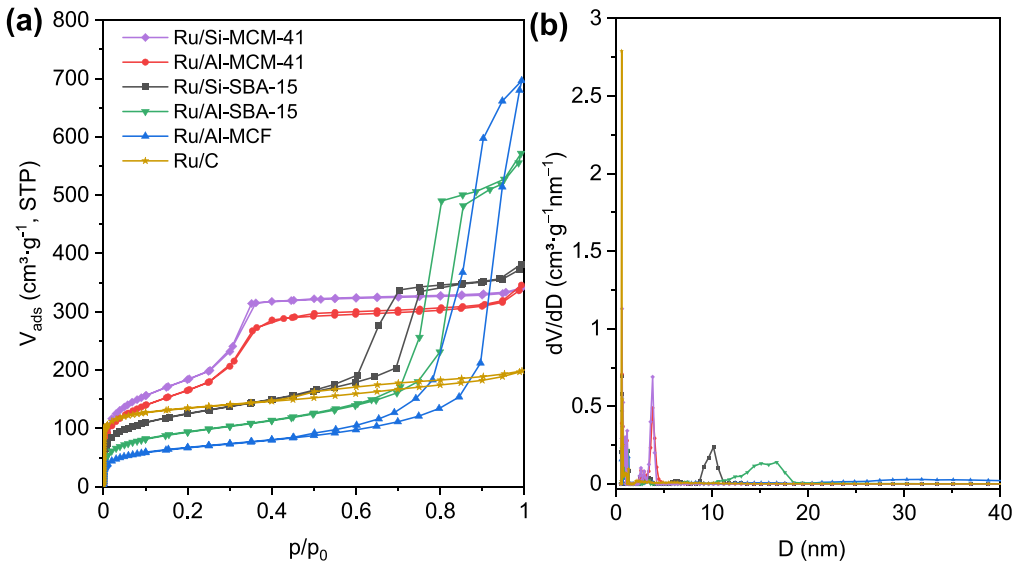

Fig. 3. Nitrogen adsorption–desorption isotherms at –196 °C (a) and pore size distribution curves (b) for MMS supported Ru nanoparticles and commercial Ru/C.

Table 2
Characteristics of the porous structure of the samples determined from nitrogen adsorption–desorption isotherms (–196 °C).

Sample	V_{micro} [a] ($cm^3 \bullet g^{-1}$)	V_{meso} [b] ($cm^3 \bullet g^{-1}$)	D_{meso} [c] (nm)	S_{meso} [d] ($m^2 \bullet g^{-1}$)	S_{BET} [e] ($m^2 \bullet g^{-1}$)
Ru/Si-MCM-41	–	0.59	3.8	640	665
Ru/Al-MCM-41	–	0.59	3.8	595	600
Ru/Si-SBA-15	0.05	0.54	10.1	340	435
Ru/Al-SBA-15	0.03	0.89	15.8	270	330
Ru/Al-MCF	0.02	1.08	31.1	185	230
Ru/C	0.13	0.15	–[f]	170	445

[a] V_{micro}, micropore volume.
[b] V_{meso}, mesopore volume.
[c] D_{meso}, mesopore diameter.
[d] S_{meso}, mesopore surface area.
[e] S_{BET}, total specific surface area.
[f] the mesopore size distribution without maximum.

Table 3
Si/Al molar ratio in the catalysts and their acidity evaluated by pyridine FTIR.

Sample	Si/Al	C_B [a] ($mmol \bullet g^{-1}$)	C_L [b] ($mmol \bullet g^{-1}$)	C_Σ [c] ($mmol \bullet g^{-1}$)	*BAS/LAS* [d]
Al-MCM-41	52	42	68	110	0.62
Ru/Al-MCM-41	54	44	76	120	0.58
Al-SBA-15	65	17	37	54	0.46
Ru/Al-SBA-15	73	22	62	84	0.36
Al-MCF	39	12	22	34	0.57
Ru/Al-MCF	68	24	43	67	0.55

[a] Brønsted acid site concentration.
[b] Lewis acid site concentration.
[c] Total acid site concentration.
[d] Brønsted-to-Lewis acid site ratio.

Ru/Al-MCF possess larger mesopores (10 – 30 nm) and mesopore volumes (up to 1.08 cm^3/g), but lower mesopore surface areas. Additionally, the textural properties of Ru/Al-MCM-41 after reaction and subsequent recovery did not change significantly. Thus, blocking of pores or a decrease in the surface area can be discarded as potential explanation for the decrease in catalytic activity.

3.1.3 Si/Al molar ratio in the samples and their acidity

Si/Al molar ratio in the obtained MMS and corresponding Ru-containing materials is similar (52 – 73, Table 3), except for Al-MCF (39). The acidic properties of aluminosilicates were investigated by pyridine adsorption with FTIR-spectral analysis. Among the investigated catalysts, Al-MCM-41 and Ru/Al-MCM-41 have the highest Brønsted and Lewis acid site concentrations (Table 3, spectra in Fig. S2). It can be suggested that in case of conventional hydrothermal synthesis under alkaline conditions, a higher fraction of Al is involved in the formation of the acid sites during conventional hydrothermal synthesis, than in the case of post-synthetic pH-adjusting method [4] for Al-SBA-15 and Al-MCF. For the synthesized catalysts, the Brønsted-to-Lewis acid site ratio is 0.36 – 0.62. An increase in Brønsted and Lewis acid site concentration in the materials after the Ru deposition can be associated with the formation of $RuOH_x$ [47] and RuO_x [48] species, respectively, on the surface of the Ru nanoparticles. The catalysts have predominantly

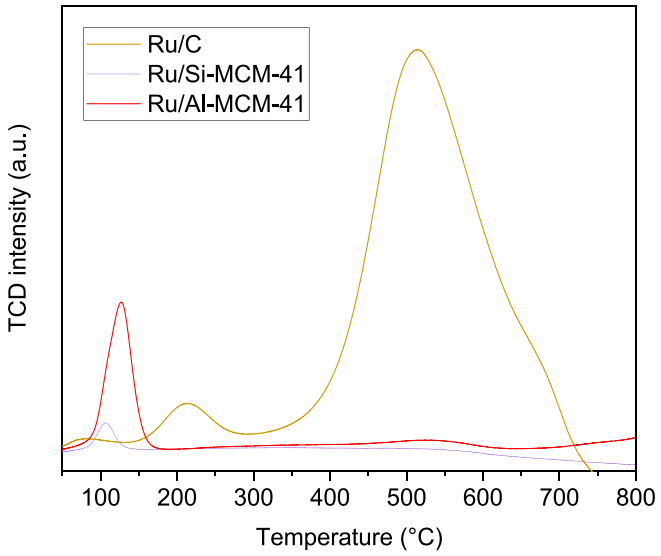

Fig. 4. TPR profiles of fresh Ru/C, Ru/Si-MCM-41 and Ru/Al-MCM-41 catalysts.

Brønsted acid sites with medium strengths as Py is almost completely desorbed after evacuation at 350 °C, Table S1. An increase in the concentration of acid sites for the initial aluminosilicates (Table 3) results in the decrease of the Ru nanoparticle size and corresponding improvement in the metal dispersion (Table 1).

3.1.4 Ru oxidation state and reduction

For the sake of comparison of the oxidation state of Ru and its interaction between the carbon and silicate/aluminosilicate supports, temperature-programmed reduction (TPR) profiles for the selected fresh catalysts, namely Ru/C, Ru/Si-MCM-41, and Ru/Al-MCM-41 were recorded. As can be seen from Fig. 4, the corresponding TPR curves for Ru/Si-MCM-41 and Ru/Al-MCM-41 possess main peaks at lower temperatures (106 and 127 °C, respectively) compared to the carbon-supported catalyst (210 – 220 °C). Lower reduction temperatures for the silica- and aluminosilica-supported Ru catalysts could indicate weaker interactions between the metal nanoparticles and support and/or higher accessibility of the precursor [49]. A broad intensive peak at ca. 500 °C for Ru/C results from methanation of the carbon support [50]. Weaker interactions in Ru/silica- and aluminosilica-supported catalysts could explain the stronger tendency to metal leaching during the reaction compared to Ru/C [18].

A higher peak intensity for Ru/Al-MCM-41 compared to Ru/Si-MCM-41 resulting in significantly higher hydrogen consumption is related to a larger Ru content in the former catalyst (Table 1). A lower intensity of the corresponding peak for Ru/C catalyst is evidently due to a larger size of the formed metal particles (Table 1).

Fig. 5 displays the XPS spectra for Ru/C and Ru/Al-MCM-41 catalysts as fresh ones and after 4 h of the reaction (90 °C and 40 bar of hydrogen pressure). The fitting data are presented in Table S2. The spectrum of Ru/Al-MCM-41 suggests that Ru is present in several oxidation states. A decrease in the relative Ru^0 percentage was observed for Ru/Al-MCM-41 after the reaction. In contrast, Ru/C exhibited a reduction in the Ru oxidation state after use in the reaction.

Previous studies have shown that the electronic state of Ru is strongly influenced by its microenvironment, that is, the solvent, promoters, and metal-support interactions [15,16,51,52]. Charge transfer between the metal and the support may generate electron-deficient Ru species, which can be beneficial in reactions that require bifunctional active sites [15]. However, for sugar hydrogenation, the decrease in metallic ruthenium on the surface negatively affects the catalytic activity.

In that sense, the presence of Ru in a lower oxidation state on the Ru/C catalyst could explain its higher activity for xylose hydrogenation and the reduction of Ru species during the reaction can be the reason for an observed increase in activity when Ru/C are used for aqueous phase hydrogenations [53–55]. Nevertheless, a special care should be taken since interpreting the Ru 3d band is challenging due to the overlapping of C-C peak with Ru species peaks and the fact that samples were exposed to air before analysis.

3.2 Experimental kinetic results

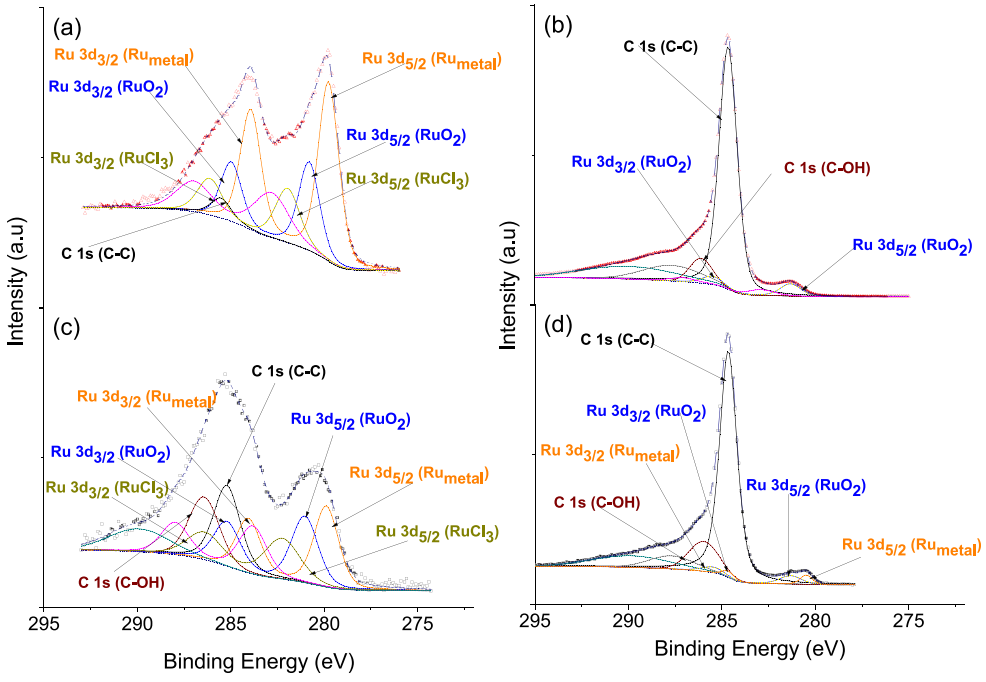

Fig. 5. XPS Ru 3d for (a) Ru/Al-MCM-41(fresh), (b) Ru/C (fresh), (c) Ru/Al-MCM-41 (used), and (d) Ru/C (used).

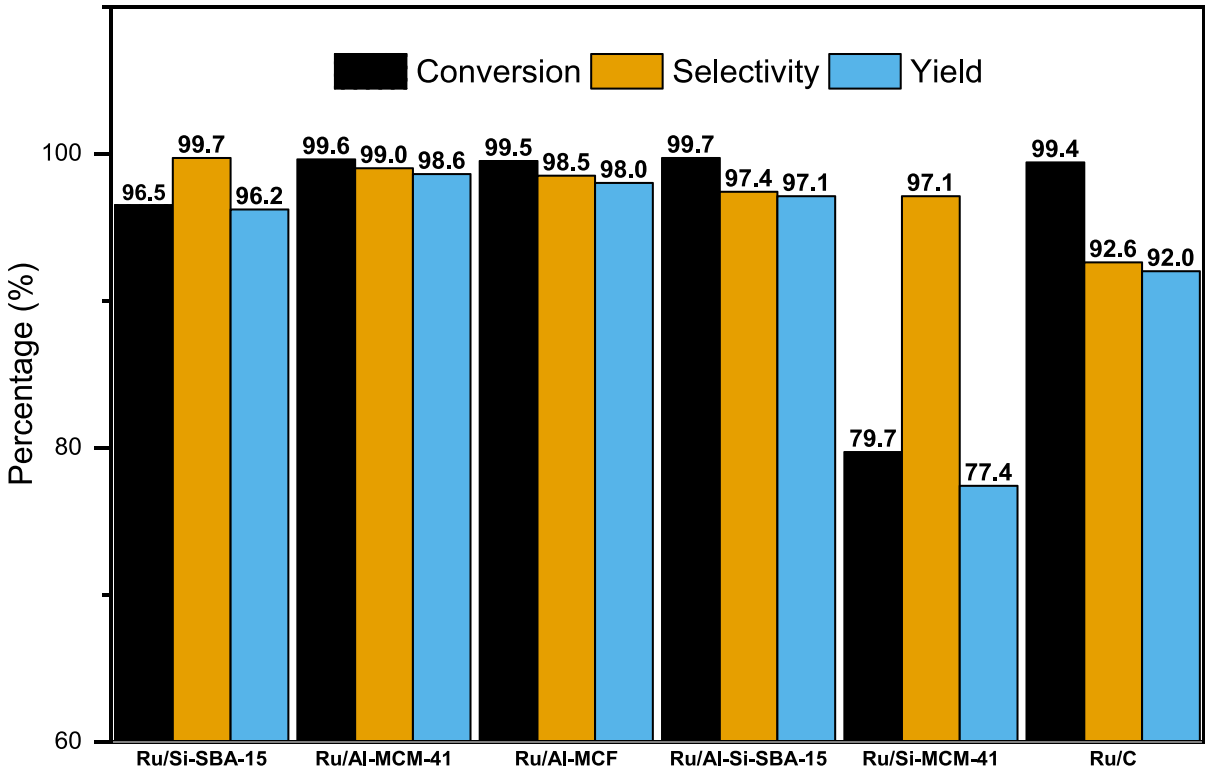

Fig. 6. Comparison of the catalysts in terms of conversion, selectivity, and xylitol yield of xylitol at 90 °C and 40 bar of hydrogen pressure. Reaction time 4 h.

3.2.1 Catalyst screening

To perform a first screening of the behavior of the catalysts, a comparison in terms of conversion, selectivity, and xylitol yield at 90 °C and 40 bar hydrogen pressure in a reaction time of 4 h is shown in Fig. 6. As expected, even at the high conversion levels obtained, between 80 and 99 %, excellent xylitol selectivity values were reached, between 93 and 99 % for all catalysts. This result is in line with the known ability of ruthenium to selectively hydrogenate carbohydrates in aqueous media [12]. Arabitol and erythritol were detected as minor by-products by HPLC. Arabitol originated from the isomerization of xylose followed by hydrogenation, whereas erythritol appeared by *retro*-aldol condensation and hydrogenation. The moderate acidity of the MMS allowed stabilization of Ru nanoparticles without significant undesired side reactions [24].

The initial turnover frequency (TOF_0) for xylose hydrogenation was computed using the initial reaction rates and ruthenium dispersion values (Table 1). No clear trends were observed in terms of the structure sensitivity (nanoparticle size), which contradicts previous observations on sugar hydrogenation using Ru/C catalysts [56,57]. On the other hand, the Ru/C catalyst displayed a considerable higher TOF value than the other catalysts, which can be related to the oxidation state of Ru on the carbon support (as revealed by XPS). In contrast, the specific activity (initial rate per gram of Ru) decreased with increasing average Ru size for the silicate and aluminosilicate-supported catalysts.

All aluminosilicate-supported catalysts exhibited higher reaction rates than the silicate-supported catalysts. Therefore, the catalyst activity can be ranked as follows: Ru/C > Ru/Al-MCM-41 > Ru/Al-MCF ≥ Ru/Al-Si-SBA-15 > Ru/Si-SBA-15 > Ru/Si-MCM-41. Ru/Al-MCM-41 displayed the highest specific activity among the prepared materials (per gram of Ru), with a performance very similar to the commercial Ru/C catalyst. Although, the initial reaction rates of Ru/Al-MCM-41 (0.047 mol•gRu^{-1}•min^{-1}) and Ru/C (0.054 mol•gRu^{-1}•min^{-1}) were close to each other, the former one exhibited a higher xylitol selectivity. Selectivity is a critical aspect to simplify the purification steps involved in the industrial production of xylitol [7].

The kinetic curves obtained for the screened catalysts are displayed in Fig. 7. At low conversion levels, the reaction was close to the zero-order with respect to xylose shifting towards the first order upon an increase of conversion. This resulted in conversion profiles featuring straight lines at the beginning, followed by bending as the reaction proceeded, finally reaching a plateau at almost complete conversion, in the of the most active catalysts.

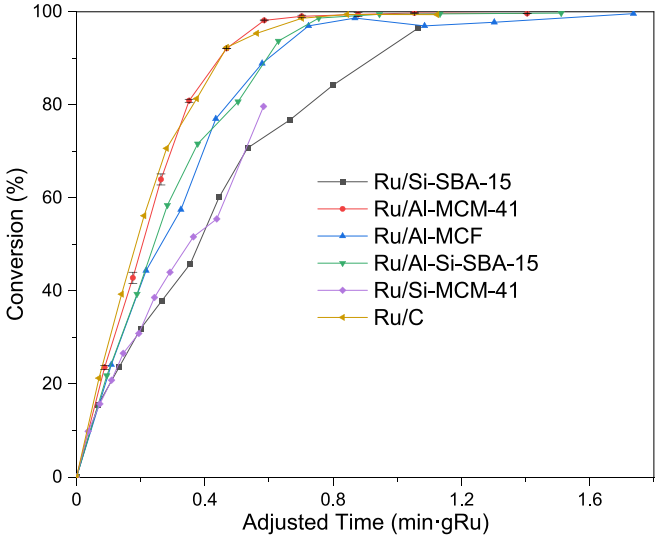

Fig. 7. Comparison of the catalysts in terms of reaction kinetics at 90 °C and 40 bar of hydrogen pressure. Reaction time 4 h.

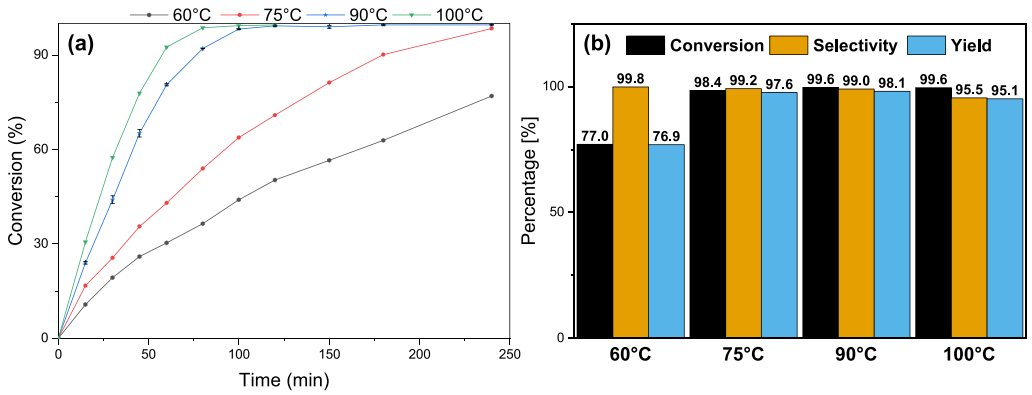

Fig. 8. Effect of the temperature on xylose hydrogenation: (a) reaction kinetics and (b) conversion, selectivity, and xylitol yield for Ru/Al-MCM-41 catalyst (0.2 g) at 40 bar of hydrogen pressure, and 4 h of reaction.

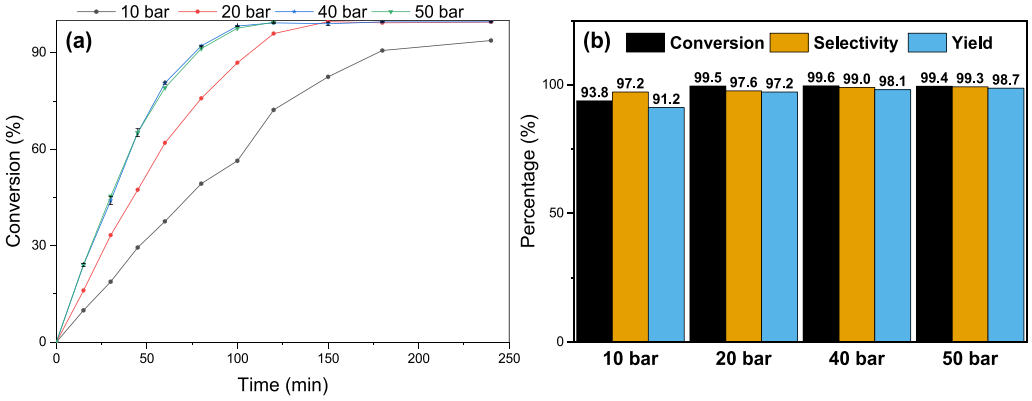

Fig. 9. Effect of hydrogen pressure on xylose hydrogenation: (a) reaction kinetics and (b) conversion, selectivity, and xylitol yield for Ru/Al-MCM-41 catalyst (0.2 g) at 90 °C, and 4 h of reaction.

3.2.2 Qualitative kinetic results

As expected, temperature had a very strong effect on the reaction rate (directly related to conversion) and on the selectivity towards xylitol. Fig. 8 shows the temperature effect on the xylose hydrogenation using Ru/Al-MCM-41. Temperatures below 75 °C resulted in slow reaction rates while the selectivity towards xylitol slightly decreases for 100 °C due to increased formation of by-products. Thus, at temperatures above 90 °C, 100 min is sufficient to achieve conversions above 99 %, while at 75 °C, 240 min (4 h) are required to achieve the same conversion. However, these high conversions at 90 °C maintain a selectivity above 99 %, while at 100 °C it drops to 95.5 %.

The effect of hydrogen pressure on the xylose hydrogenation rate with Ru/Al-MCM-41is exemplified in Fig. 9. At pressures below 20 bar, the hydrogen pressure exhibited a strong effect on the hydrogenation rate, which is consistent with previous studies on xylose hydrogenation [23,58] and other monomeric sugars [17,18,54]. However, the effect became rather weak at pressures exceeding 40 bar. These results indicate a strong hydrogen adsorption on the Ru surface, which becomes saturated at high concentrations of hydrogen in the liquid phase, resulting in a zero-order reaction rate with respect to hydrogen.

Fig. 10 shows a comparison with the fresh and used Ru/Al-MCM-41 catalysts. A decrease in the activity equivalent to c.a. 30 % the initial rate was observed. The catalyst deactivation can mainly be attributed to ruthenium leaching as displayed in Table 4; from this table is evident

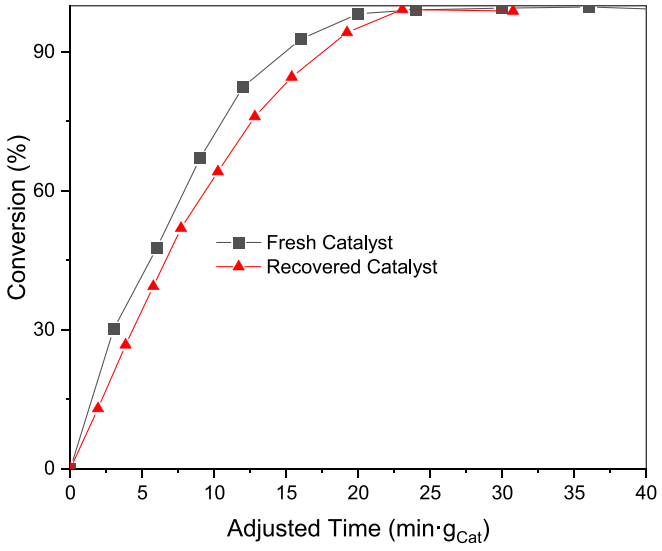

Fig. 10. Comparison of the fresh and recovered Ru-Al-MCM-41 catalyst in the xylose hydrogenation at 90 °C and 40 bar of hydrogen pressure.

Table 4
Leaching of Ru from Ru/Al-MCM-41 catalyst after 4 h of reaction determined by ICP-EOS.

Temperature (°C)	Ru concentration in the reaction mixture [a] (mg•L^{-1})	Ru leached (%) [b]
75	<0.03	–
90	0.55	1.20
100	0.97	2.15

[a] Concentration of Ru in the reaction mixture after each experiment.
[b] Percentage of Ru leached with respect to the original Ru content in the catalyst.

that the degree of Ru dissolution is strongly influenced by the reaction temperature, hence the operational conditions should be adjusted to ensure reusability of the catalyst in practical applications. Nevertheless, the xylitol selectivity and yield at the final conversion did not change significantly.

4. Kinetic modelling

4.1. Model assumptions

The data obtained for Ru/MCM-41 were used for parameter estimation by comparing two different models (denoted model 1 and model 2 and described below). The general assumptions used to derive the models are listed below.

- The high stirring rate (1000 rpm) used during the experiments and the small size of the catalyst particles (≤40 μm, see Fig. S4) ensured that the reaction proceeded in the absence of external and internal mass transfer limitations. The Weisz-Prater criterion was applied (see Electronic Supporting Information S.2.1) to confirm the absence of internal mass transfer limitations.
- The liquid-phase reaction volume was assumed constant, since the equivalent mass withdrawn as samples from the reactor was less than 6 %.
- Only formation of xylitol was considered for quantitative modelling, because of the high values of selectivity. The formation of by-products could thus be neglected.
- The hydrogen concentration in the liquid phase is proportional to the hydrogen pressure for low sugar concentration values as the one used in this work (0.13 mol•L^{-1}). Previous studies have demonstrated the validity of Henry's law for dilute sugar solutions in aqueous media [59].
- The experiments were conducted under isothermal conditions, the reaction enthalpy value is relatively low [60], and low xylose concentrations were used in this study. Consequently, the energy balance was neglected and not considered in the model.
- The experiments were performed under a constant pressure of hydrogen regulated by a controller and equilibrium concentrations of dissolved hydrogen were considered to prevail in the liquid phase. Therefore, the mass balance of hydrogen was discarded, and the observed reaction rates were assumed and modelled.

4.2. Derivation of rate equations

4.2.1. Model 1 – Xylose and hydrogen non-competitive adsorption

The first model (Scheme 1) implemented with the experimental data is the non-competitive adsorption model, which assumes that the reactants (xylose and hydrogen) are adsorbed on different active sites on the catalyst (denoted by * and *′, respectively), which is a reasonable approximation because of the size differences between xylose (a five-carbon carbohydrate) and hydrogen. This approach has been successfully applied to describe the kinetics of hydrogenation of monomeric and dimeric sugars on Ru-based catalysts in previous studies [18,58,61,62] as well as in other reactions characterized by substantial differences in size among the reactants involved, such as ethyl benzoylformate

1. $X+* \equiv X*$
2. $H_2+2*' \leftrightarrow 2H*'$
3. $X* +2H*' \equiv X_{OH}+*+2*'$

Scheme 1. Model 1 proposed for xylose hydrogenation.

1. $X*+H_2 \leftrightarrow X*H_2$
2. $X*H_2 \rightarrow X_{OH}*$
3. $X_{OH}*+X \equiv X_{OH}+X*$

Scheme 2. Model 2 proposed for xylose hydrogenation.

hydrogenation [63] and 1-phenyl-1,2-propanedione hydrogenation [64].

The rate expression for xylose hydrogenation to xylitol is presented in eq. (3), where κ_{ave} is a merged pre-exponential factor in the rate constant and the adsorption equilibrium constant of xylose and hydrogen at the average experimental temperature ($\overline{T} = 354$ K) and E_A is the merged activation energy of the catalytic process, described by the Arrhenius and van't Hoff laws. The adsorption is considered to follow the Langmuir model, with K_X and K_{H_2} being the adsorption constants for xylose and atomic hydrogen, respectively. The reaction between xylose and two hydrogen adsorbed atoms on the catalyst surface is assumed to be the rate-determining step. The derivation of the rate equation is available in the section S.3.2 of the Electronic Supporting Information.

$$r = \frac{\kappa_{ave} \cdot e^{\frac{E_A}{R}\left(\frac{1}{\overline{T}}-\frac{1}{T}\right)} \cdot C_X \cdot P_{H_2}}{(1 + K_X \cdot C_X) \cdot \left(1 + \sqrt{K_{H_2} \cdot P_{H_2}}\right)^2} \tag{3}$$

4.2.2. Model 2 – Xylose-hydrogen intermediate formation

Scheme 2 shows an alternative mechanism for xylose hydrogenation. This model assumes the formation of an intermediate between xylose and hydrogen on the catalyst surface, which is denoted by $X*H_2$. In the second step, the intermediate is converted into xylitol, and an exchange between the product and xylose from the liquid phase takes place in the third step, releasing the product, i.e., xylitol. Consequently, the adsorption strength of the product influences the reaction rate. This model has been developed and applied previously for hydrogenation of olefinic compounds [65,66].

After applying the adsorption–desorption quasi-equilibria on step 3, the coverage of xylitol is obtained from

$$\theta_{XOH} = \frac{\theta_x \cdot C_{XOH}}{K_3 \cdot C_x} \tag{4}$$

Applying the quasi-steady state approximation for steps 1 and 2, i.e., $r = r_1 = r_2$, eq. (5) is obtained,

$$k_{+1} \cdot \theta_X \cdot P_{H_2} - k_{-1} \cdot \theta_{X-H_2} - k_{+2} \cdot \theta_{X-H_2} = 0 \tag{5}$$

from which the surface coverage of the intermediate is solved,

$$\theta_{X-H_2} = \frac{k_{+1} \cdot \theta_X \cdot P_{H_2}}{k_{-1} + k_{+2}} \tag{6}$$

The site balance is written as it follows,

$$\theta_X + \theta_{XOH} + \theta_{X\text{-}H_2} = 1 \tag{7}$$

The site balance can be expressed as a function of the coverage of xylose by inserting eqs. (4) and (6) in eq. (7), which yields

$$\theta_X + \frac{C_{XOH}}{K_3 \cdot C_x} \cdot \theta_X + \frac{k_{+1} \cdot P_{H_2}}{k_{-1} + k_{+2}} \cdot \theta_X = 1 \tag{8}$$

from where the xylose coverage is obtained,

$$\theta_X = \frac{1}{1 + \frac{C_{XOH}}{K_3 \cdot C_x} + \frac{k_{+1} \cdot P_{H_2}}{k_{-1} + k_{+2}}} \tag{9}$$

The rate of the catalytic process can be described as the rate of the second step,

$$r = k_{+2} \cdot \theta_{X-H_2} \quad (10)$$

Insertion of eqs. (7) and (9) in the rate eq. (10) and some algebraic rearrangement give the final form of the rate eq. (11).

$$r = \frac{\frac{k_{+2} \cdot k_{+1}}{k_{-1}+k_{+2}} \cdot C_x \cdot P_{H_2}}{C_X + \frac{1}{K_3} \cdot C_{XOH} + \frac{k_{+1}}{k_{-1}+k_{+2}} \cdot C_x \cdot P_{H_2}} \quad (11)$$

The kinetic and adsorption parameters are expected to follow the laws of Arrhenius and van't Hoff as expressed by eqs. (12)–(16), with the average T of 354 K

$$k_{+1} = k_{+1,ave} \cdot e^{\frac{E_{+1}}{R}\left(\frac{1}{T}-\frac{1}{T}\right)} \quad (12)$$

$$k_{-1} = k_{-1,ave} \cdot e^{\frac{E_{-1}}{R}\left(\frac{1}{T}-\frac{1}{T}\right)} \quad (13)$$

$$k_{+2} = k_{+2,ave} \cdot e^{\frac{E_{+2}}{R}\left(\frac{1}{T}-\frac{1}{T}\right)} \quad (14)$$

4.3. Mass balance equations and numerical solution strategy

The transient mass balances for xylose and xylitol in the liquid phase for a batch reactor are given in eqs. (15) and (16), respectively, where ρ_B is the catalyst bulk density, i.e., the ratio of the ruthenium mass to the reaction volume, and r is the reaction rate, as defined by eqs. (3) and (11), depending on the model selected (Model 1 or Model 2).

$$\frac{dC_X}{dt} = -r \cdot \rho_B \quad (15)$$

$$\frac{dC_{X_{OH}}}{dt} = r \cdot \rho_B \quad (16)$$

The parameters of both models were estimated by minimizing the objective function presented in eq. (17) using the Nelder-Mead optimization algorithm coupled with the system of ordinary differential eqs. (15) and (16) which were solved by the LSODA routine implemented in Python.

$$Q = \sum_{i=1}^{n} \left(C_{Exp,i} - C_{Calc,i}\right)^2 \quad (17)$$

The coefficient of determination (R^2) was computed with eq. (18) to evaluate the goodness of fit, which compares the model performance with the mean concentration. The value of R^2 can vary between 0 and 100 %.

$$R^2 = \left(1 - \frac{\sum_{i=1}^{n}\left(C_{Exp,i} - C_{Calc,i}\right)^2}{\sum_{i=1}^{n}\left(C_{Exp,i} - C_{mean,i}\right)^2}\right) \cdot 100 \quad (18)$$

4.4. Modelling results

4.4.1. Model 1 – Xylose and hydrogen non-competitive adsorption

The estimated parameters are listed in Table 5. As expected, model 1 (non-competitive adsorption model) successfully describes the experimental data with a high degree of explanation (R^2 = 98.96 %). The activation energy value of 43.21 kJ/mol corresponds to previously reported values for Ru-based catalysts (40–60 kJ•mol^{-1}) [18,23,58]. The value of K_X = 14.29 L/mol indicates strong adsorption of xylose. Table 6 shows the correlation matrix for the estimated parameters, giving in all cases values for the Pearson correlation coefficient less than 0.9. The strongest correlation was between $k_{81°C}$ and K_X (0.891) and K_{H2} (0.378), indicating that the specific reaction rate is positively correlated with the adsorption parameters, which is a characteristic feature for this kind of models, since the parameters in the nominator and the denominator can compensate each other.

Table 5
Kinetic parameters estimated for the non-competitive model 1 (NCAM).

Parameter	Value	Relative Error (%)	Units
κ_{ave}	0.047	6.0	L•gRu^{-1}•min^{-1} bar^{-1}
E_A	43.21	1.3	kJ•mol^{-1}
K_X	14.29	10	L•mol^{-1}
K_{H_2}	0.039	5.0	bar^{-1}
Q	0.003	–	mol•L^{-1}
R^2	98.96	–	%

The model describes rather well the concentration profiles as well as the effect of temperature and hydrogen pressure on the hydrogenation rate as shown in Fig. S7 and Fig. S8, respectively.

4.4.2. Model 2 – Xylose-hydrogen intermediate formation

Table 7 lists the obtained parameters for model 2 with the correlation matrix presented in Table 8. In general, a high degree of description of the experimental data (R^2 = 98.98%) was achieved and the influence of both the temperature and hydrogen pressure is accurately described by the model (Fig. 11 and Fig. 12, respectively). It is comparable with the description achieved with Model 1.

The values of the fitted parameters observed in Table 7 indicate that the formation of the intermediate xylose-hydrogen on the active site is faster compared to the backward reaction (e.g., $k_{+1,ave} \cdot P_{H_2}$ = 0.32 $mol\ \mathrm{min}^{-1} \cdot g_{Ru}^{-1} \cdot bar^{-1}$ at 40 bar). The value of the adsorption constant (K_3) suggests that the adsorption strength of xylitol on the active sites is lower compared to xylose adsorption, which agrees with the previous modelling results of sugar hydrogenation [18]. In this case, the correlation among parameters is low in general. However, it can be seen some correlation between the activation energies E_{+1} and E_{-1} (0.358) and E_{+1} and E_{+2} (-0.518), which is normal as the value of the forward activation energy can be somehow compensated by the backward

Table 6
Correlation matrix of the parameters for the model 1.

	κ_{ave}			
κ_{ave}	1	E_A		
E_A	−0.074	1	K_X	
K_X	0.891	−0.045	1	K_{H_2}
K_{H_2}	0.378	−0.065	−0.067	1

Table 7
Kinetic parameters estimated for Model 2.

Parameter	Value	Relative Error, (%)	Units
$k_{+1,ave}$	0.008	0.2	mol min^{-1}•g$_{Ru}^{-1}$•bar^{-1}
E_{+1}	58.61	0.6	kJ•mol^{-1}
$k_{-1,ave}$	0.14	4.8	mol min^{-1}•g$_{Ru}^{-1}$
E_{-1}	20.26	1.3	kJ•mol^{-1}
$k_{+2,ave}$	0.053	2.1	mol min^{-1}•g$_{Ru}^{-1}$•bar^{-1}
E_{+2}	23.84	1.4	kJ•mol^{-1}
K_3	1.14	2.7	–
Q	0.003	–	L^2•mol^{-2}
R^2	98.98	–	%

Table 8
Correlations matrix of the parameters for model 2.

	$k_{+1,ave}$						
$k_{+1,ave}$	1	E_{+1}					
E_{+1}	−0.004	1	$k_{-1,ave}$				
$k_{-1,ave}$	0.130	0.035	1	E_{-1}			
E_{-1}	0.004	0.358	0.031	1	$k_{2,ave}$		
$k_{+2,ave}$	0.063	0.044	0.897	0.036	1	E_2	
E_2	−0.014	−0.518	−0.155	−0.052	−0.187	1	K_3
K_3	0.023	0.012	0.312	−0.001	0.014	−0.013	1

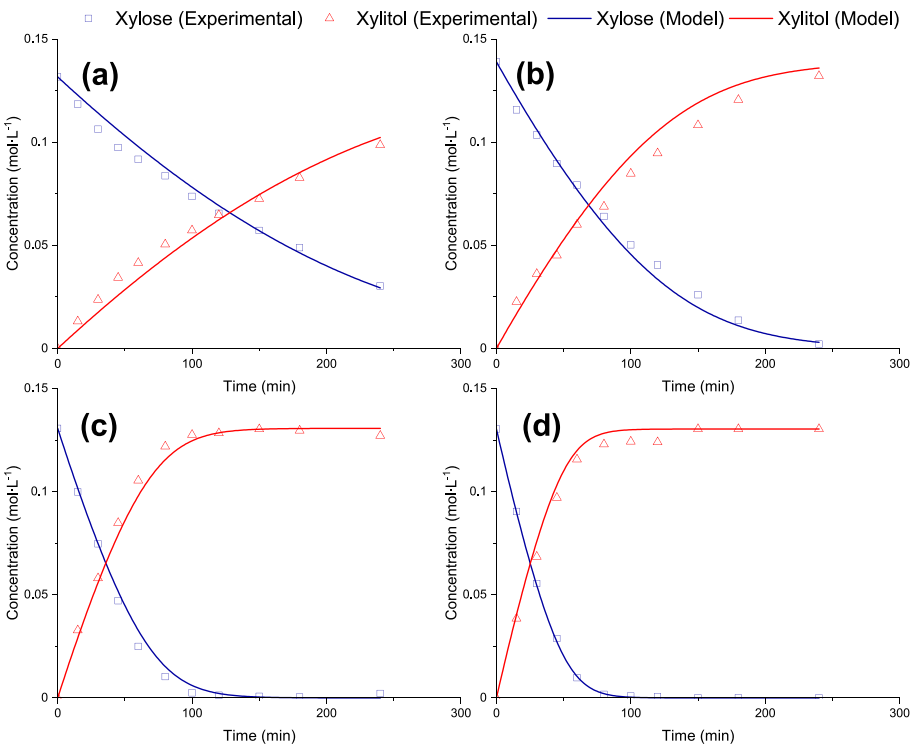

Fig. 11. Concentration curves in hydrogenation of xylose at 40 bar hydrogen pressure on Ru-Al-MCM-41 catalyst at (a) 60 °C, (b) 75 °C, (c) 90 °C, (d) 100 °C (model 2). Experimental points- symbols, calculations-lines.

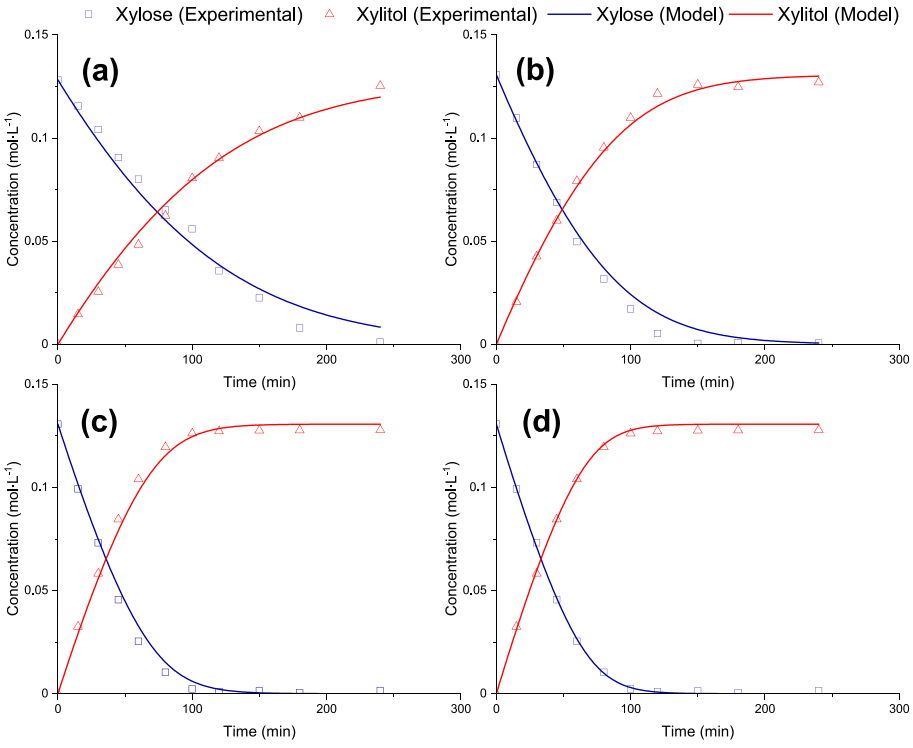

Fig. 12. Concentration curves in hydrogenation of xylose at 90 °C on catalysts Ru-Al-MCM-41 at (a) 10 bar, (b) 20 bar, (c) 40 bar, (d) 50 bar (Model 2). Experimental points- symbols, calculations-lines.

reaction. Similarly, as can be expected, a correlation between k_{-1} and k_2 exists (0.897) as both parameters are competing for the same sites, as it can be seen in eq. (5).

Model 2 explains the zero order in xylose and hydrogen simultaneously as isomerization of the complex $X*H_2$, considering that the adsorption of the product (xylitol) is limited, unlike the model 1, which predicts zero order with respect to hydrogen at the maximum coverage of the adsorption sites devoted to hydrogen and with respect to xylose at

the maximum coverage of the sites corresponding to xylose adsorption.

5. Conclusions

Ruthenium-based catalysts supported on different silicate and aluminosilicate mesoporous molecular sieves were synthesized and characterized in terms of morphology, textural properties, ruthenium content, and Ru nanoparticle size distribution. In general, the aluminosilicate-supported catalysts displayed a higher Ru loading along with a narrower particle size distribution. The prepared catalysts were used in selective xylose hydrogenation to xylitol and compared with a commercial Ru/C catalyst. The specific catalytic activity followed the sequence: Ru/C > Ru/Al-MCM-41 > Ru/Al-MCF ≥ Ru/Al-Si-SBA-15 > Ru/Si-SBA-15 > Ru/Si-MCM-41.Overall, the synthetized materials displayed a xylitol selectivity exceeding 99 % compared to 92.6 % selectivity for the commercial Ru/C catalyst. High selectivity is a critical aspect to simplify the purification steps involved in the industrial production of xylitol.

The most active catalyst among the synthesized materials was Ru/Al-MCM-41 with an improved performance compared to Ru/C due to a higher selectivity to xylitol. Higher activity of Ru/C (expressed as initial reaction rates) can be explained in terms of stronger interactions between Ru and carbon (as revealed by TPR) that prevents metal leaching and a lower oxidation state of ruthenium on this support as suggested by XPS results.

The kinetic data obtained with Ru/Al-MCM-41 were modelled by two approaches: non-competitive adsorption of xylose and hydrogen (model 1) and a model that presumes formation of an intermediate on the catalyst surface (model 2). In model 1, the rate can simultaneously be zero order with respect to one component (e.g., xylose) and deviate from zero order for the other (hydrogen). In contrast, for model 2, the zero reaction order stems from surface isomerization of the xylose-dihydrogen complex. Despite these differences, both models displayed similar performances in terms of the data fitting and description of the temperature and pressure effects.

CRediT authorship contribution statement

German Araujo-Barahona: Writing – original draft, Investigation, Data curation. **Nataliya Shcherban:** Writing – original draft, Methodology, Investigation, Conceptualization. **Kari Eränen:** Project administration, Methodology. **Ivan Kopa:** Investigation. **Igor Bezverkhyy:** Investigation. **Mark Martínez-Klimov:** Investigation. **Zuzana Vajglová:** Investigation. **Atte Aho:** Investigation. **Juan García-Serna:** Resources, Conceptualization. **Tapio Salmi:** Writing – review & editing, Supervision, Resources, Project administration, Methodology, Conceptualization. **Dmitry Yu. Murzin:** Supervision, Methodology, Conceptualization, Writing – review & editing.

Declaration of competing interest

The authors declare that they have no known competing financial interests or personal relationships that could have appeared to influence the work reported in this paper.

Data availability

Data will be made available on request.

Acknowledgements

This work is part of the activities financed by the Academy of Finland through the Academy Professor grants 319002, 320115, 345053 (Tapio Salmi). Economic support from Åbo Akademi University Graduate School (German Araujo Barahona) is gratefully acknowledged. Nataliya Shcherban acknowledges U.S. Department of Energy, Office of Science, Office of Basic Energy Sciences, Catalysis Science, under Award Number DE-SC0021041 for supporting X-ray diffraction and pyridine adsorption with FTIR-spectral analysis, and the National Research Foundation of Ukraine which funded the materials synthesis through the project "New effective zeolite catalysts for environmentally friendly processes of the conversion of renewable raw materials into valuable organic compounds" (project number 2020.02/0335). Juan García Serna wish to thank Agencia Estatal de Investigación, Unión Europea-Next Generation UE, Plan de Recuperación, Transformación y Resiliencia, Ministerio de Ciencia e Innovación (MICINN) and Universidad de Valladolid for funding in projects TED2021-129837B-C42 and PID2019-105975 GB-I00 and FEDER Funds and Junta de Castilla y León (Consejería de Educación) project CLU-2019-04. Authors are grateful to the Materials Research Infrastructure/Department of Physics and Astronomy, University of Turku (XPS spectrometer) and to the Electron Microscopy Laboratory, Institute of Biomedicine, University of Turku, and Biocenter Finland.

Appendix A. Supplementary data

Supplementary data to this article can be found online at https://doi.org/10.1016/j.cej.2024.150019.

References

[1] C.D. Pinales-Márquez, R.M. Rodríguez-Jasso, R.G. Araújo, A. Loredo-Treviño, D. Nabarlatz, B. Gullón, H.A. Ruiz, Circular bioeconomy and integrated biorefinery in the production of xylooligosaccharides from lignocellulosic biomass: a review, Ind. Crop. Prod. 162 (2021) 113274, https://doi.org/10.1016/j.indcrop.2021.113274.

[2] P. Mäki-Arvela, T. Salmi, B. Holmbom, S. Willför, D.Y. Murzin, Synthesis of sugars by hydrolysis of hemicelluloses- a review, Chem. Rev. 111 (2011) 5638–5666, https://doi.org/10.1021/cr2000042.

[3] A.M. Ruppert, K. Weinberg, R. Palkovits, Hydrogenolysis goes bio: from carbohydrates and sugar alcohols to platform chemicals, Angewandte Chemie - International Edition 51 (2012) 2564–2601, https://doi.org/10.1002/anie.201105125.

[4] D.Y. Murzin, A. Duque, K. Arve, V. Sifontes, A. Aho, K. Eränen, T. Salmi, Catalytic hydrogenation of sugars, RSC Green Chemistry (2016), https://doi.org/10.1039/9781782622079-00089.

[5] D.Y. Murzin, E. Daigue, R. Slotte, D.A. Sladkovskiy, T. Salmi, Techno-economic analysis for production of L-arabitol from L-arabinose, Chem. Eng. Technol. 43 (2020) 1260–1267, https://doi.org/10.1002/ceat.202000125.

[6] B. Zada, M. Chen, C. Chen, L. Yan, Q. Xu, W. Li, Q. Guo, Y. Fu, Recent advances in catalytic production of sugar alcohols and their applications, Sci. China Chem. 60 (2017) 853–869, https://doi.org/10.1007/s11426-017-9067-1.

[7] F.M. Jofre, F.W. Bordini, I. de Andrade Bianchini, S. de Souza Queiroz, T. da Silva Boaes, A.F. Hernández-Pérez, M. das G. de Almeida Felipe, Xylitol and sorbitol: production routes, challenges and opportunities in biorefineries integration, in: A. K. Chandel, F. Segato (Eds.), Production of Top 12 Biochemicals Selected by USDOE from Renewable Resources: Status and Innovation, Elsevier, 2022: pp. 233–268. https://doi.org/10.1016/B978-0-12-823531-7.00013-5.

[8] Research and Markets, Xylitol Market: Global Industry Trends, Share, Size, Growth, Opportunity and Forecast 2022-2027, 2021. https://www.researchandmarkets.com/reports/5647789/xylitol-market-global-industry-trends-share?w=4 (accessed November 27, 2022).

[9] D.Y. Murzin, A. Duque, K. Arve, V. Sifontes, A. Aho, K. Eränen, T. Salmi, Catalytic hydrogenation of sugars, in: RSC Green Chemistry, The Royal Society of Chemistry, 2016: pp. 89–133. https://doi.org/10.1039/9781782622079-00089.

[10] B. Chen, U. Dingerdissen, J.G.E. Krauter, H.G.J. Lansink Rotgerink, K. Möbus, D. J. Ostgard, P. Panster, T.H. Riermeier, S. Seebald, T. Tacke, H. Trauthwein, New developments in hydrogenation catalysis particularly in synthesis of fine and intermediate chemicals, Appl Catal A Gen 280 (2005) 17–46, https://doi.org/10.1016/j.apcata.2004.08.025.

[11] C. Michel, P. Gallezot, Why is ruthenium an efficient catalyst for the aqueous-phase hydrogenation of biosourced carbonyl compounds? ACS Catal. 5 (2015) 4130–4132, https://doi.org/10.1021/acscatal.5b00707.

[12] M.A. Ramzan, R. Wischert, S.N. Steinmann, C. Michel, Toward a realistic surface state of ru in aqueous and gaseous environments, J. Phys. Chem. Lett. 14 (2023) 4241–4246, https://doi.org/10.1021/acs.jpclett.3c00313.

[13] A. Seretis, P. Diamantopoulou, I. Thanou, P. Tzevelekidis, C. Fakas, P. Lilas, G. Papadogianakis, Recent advances in ruthenium-catalyzed hydrogenation reactions of renewable biomass-derived levulinic acid in aqueous media, Front. Chem. 8 (2020) 1–22, https://doi.org/10.3389/fchem.2020.00221.

[14] M. Akram, S.U.A. Bhutto, S. Aftab, F. Wang, X. Xu, M. Xia, Ruthenium based with carbon supported catalysts for the catalytic transfer hydrogenation of furfural: a review, Nano Energy 117 (2023) 108808, https://doi.org/10.1016/j.nanoen.2023.108808.

[15] Z. Yu, N. Ji, J. Xiong, Y. Han, X. Li, R. Zhang, Y. Qiao, M. Zhang, X. Lu, Ultrafine ruthenium clusters Shell-embedded hollow carbon spheres as nanoreactors for channel microenvironment-modulated furfural tandem hydrogenation, Small 18 (2022) 2201361, https://doi.org/10.1002/smll.202201361.
[16] S. El Sayed, A. Bordet, C. Weidenthaler, W. Hetaba, K.L. Luska, W. Leitner, Selective hydrogenation of benzofurans using ruthenium nanoparticles in Lewis acid-modified ruthenium-supported ionic liquid phases, ACS Catal. 10 (2020) 2124–2130, https://doi.org/10.1021/acscatal.9b05124.
[17] E. Crezee, B.W. Hoffer, R.J. Berger, M. Makkee, F. Kapteijn, J.A. Moulijn, Three-phase hydrogenation of D-glucose over a carbon supported ruthenium catalyst - mass transfer and kinetics, Appl. Catal. A 251 (2003) 1–17, https://doi.org/10.1016/S0926-860X(03)00587-8.
[18] V.A. Sifontes Herrera, O. Oladele, K. Kordás, K. Eränen, J.P. Mikkola, D.Y. Murzin, T. Salmi, Sugar hydrogenation over a Ru/C catalyst, J. Chem. Technol. Biotechnol. 86 (2011) 658–668, https://doi.org/10.1002/jctb.2565.
[19] J.L. Santos, L.M. Sanz-Moral, A. Aho, S. Ivanova, D.Y. Murzin, M.A. Centeno, Structure effect of modified biochar in Ru/C catalysts for sugar mixture hydrogenation, Biomass Bioenergy 163 (2022) 106504, https://doi.org/10.1016/j.biombioe.2022.106504.
[20] S.G. Akpe, S.H. Choi, H.C. Ham, Conversion of cyclic xylose into xylitol on ru, pt, pd, ni, and rh catalysts: a density functional theory study, PCCP 23 (2021) 26195–26208, https://doi.org/10.1039/d1cp04660h.
[21] K. Van Gorp, E. Boerman, C.V. Cavenaghi, P.H. Berben, Catalytic hydrogenation of fine chemicals: sorbitol production, Catal. Today 52 (1999) 349–361, https://doi.org/10.1016/S0920-5861(99)00087-5.
[22] B.W. Hoffer, E. Crezee, P.R.M. Mooijman, A.D. Van Langeveld, F. Kapteijn, J. A. Moulijn, Carbon supported ru catalysts as promising alternative for raney-type ni in the selective hydrogenation of D-glucose, Catal. Today 79–80 (2003) 35–41, https://doi.org/10.1016/S0920-5861(03)00040-3.
[23] T.N. Pham, A. Samikannu, A.R. Rautio, K.L. Juhasz, Z. Konya, J. Wärnå, K. Kordas, J.P. Mikkola, Catalytic hydrogenation of d-xylose over ru decorated carbon foam catalyst in a SpinChem® rotating bed reactor, Top. Catal. 59 (2016) 1165–1177, https://doi.org/10.1007/s11244-016-0637-4.
[24] L. Vilcocq, A. Paez, V.D.S. Freitas, L. Veyre, P. Fongarland, R. Philippe, Unexpected reactivity related to support effects during xylose hydrogenation over ruthenium catalysts, RSC Adv. 11 (2021) 39387–39398, https://doi.org/10.1039/d1ra08193d.
[25] X. Guo, X. Wang, J. Guan, X. Chen, Z. Qin, X. Mu, M. Xian, Selective hydrogenation of D-glucose to D-sorbitol over RU/ZSM-5 catalysts, cuihua xuebao/chinese, J. Catal. 35 (2014) 733–740, https://doi.org/10.1016/s1872-2067(14)60077-2.
[26] A. Romero, E. Alonso, Á. Sastre, A. Nieto-Márquez, Conversion of biomass into sorbitol: cellulose hydrolysis on MCM-48 and d-glucose hydrogenation on RU/MCM-48, Microporous Mesoporous Mater. 224 (2016) 1–8, https://doi.org/10.1016/j.micromeso.2015.11.013.
[27] J.A. Melero, J. Moreno, J. Iglesias, G. Morales, J.L.G. Fierro, R. Sánchez-Vázquez, A. Cubo, B. García, Ru-ZrO2-SBA-15 as efficient and robust catalyst for the aqueous phase hydrogenation of glucose to sorbitol, Mol. Catal. 484 (2020) 110802, https://doi.org/10.1016/j.mcat.2020.110802.
[28] C.T. Kresge, M.E. Leonowicz, W.J. Roth, J.C. Vartuli, J.S. Beck, Ordered mesoporous molecular sieves synthesized by a liquid-crystal template mechanism, Nature 359 (1992) 710–712, https://doi.org/10.1038/359710a0.
[29] P.T. Tanev, T.J. Pinnavaia, Mesoporous silica molecular sieves prepared by ionic and neutral surfactant templating: a comparison of physical properties, Chem. Mater. 8 (1996) 2068–2079, https://doi.org/10.1021/cm950549a.
[30] D. Zhao, J. Feng, Q. Huo, N. Melosh, G.H. Fredrickson, B.F. Chmelka, G.D. Stucky, Triblock copolymer syntheses of mesoporous silica with periodic 50 to 300 angstrom pores, Science (1979) 279 (1998). https://doi.org/10.1126/science.279.5350.548.
[31] S. Wu, Y. Han, Y.C. Zou, J.W. Song, L. Zhao, Y. Di, S.Z. Liu, F.S. Xiao, Synthesis of heteroatom substituted SBA-15 by the "pH-adjusting" method, Chem. Mater. 16 (2004) 486–492, https://doi.org/10.1021/cm0343857.
[32] Q. Li, J. Yang, D. Feng, Z. Wu, Q. Wu, S.S. Park, C.S. Ha, D. Zhao, Facile synthesis of porous carbon nitride spheres with hierarchical three-dimensional mesostructures for CO2 capture, Nano Res. 3 (2010) 632–642, https://doi.org/10.1007/s12274-010-0023-7.
[33] G. Bergeret, P. Gallezot, Particle Size and Dispersion Measurements, in: Handbook of Heterogeneous Catalysis, 2nd ed., Wiley-VCH , 2008: pp. 738–765. https://doi.org/10.1002/9783527610044.hetcat0038.
[34] J.W.M. Osterrieth, J. Rampersad, D. Madden, N. Rampal, L. Skoric, B. Connolly, M. D. Allendorf, V. Stavila, J.L. Snider, R. Ameloot, J. Marreiros, C. Ania, D. Azevedo, E. Vilarrasa-Garcia, B.F. Santos, X.H. Bu, Z. Chang, H. Bunzen, N.R. Champness, S. L. Griffin, B. Chen, R.B. Lin, B. Coasne, S. Cohen, J.C. Moreton, Y.J. Colón, L. Chen, R. Clowes, F.X. Coudert, Y. Cui, B. Hou, D.M. D'Alessandro, P.W. Doheny, M. Dincă, C. Sun, C. Doonan, M.T. Huxley, J.D. Evans, P. Falcaro, R. Ricco, O. Farha, K.B. Idrees, T. Islamoglu, P. Feng, H. Yang, R.S. Forgan, D. Bara, S. Furukawa, E. Sanchez, J. Gascon, S. Telalović, S.K. Ghosh, S. Mukherjee, M.R. Hill, M.M. Sadiq, P. Horcajada, P. Salcedo-Abraira, K. Kaneko, R. Kukobat, J. Kenvin, S. Keskin, S. Kitagawa, K. ichi Otake, R.P. Lively, S.J.A. DeWitt, P. Llewellyn, B. V. Lotsch, S.T. Emmerling, A.M. Pütz, C. Martí-Gastaldo, N.M. Padial, J. García-Martínez, N. Linares, D. Maspoch, J.A. Suárez del Pino, P. Moghadam, R. Oktavian, R.E. Morris, P.S. Wheatley, J. Navarro, C. Petit, D. Danaci, M.J. Rosseinsky, A.P. Katsoulidis, M. Schröder, X. Han, S. Yang, C. Serre, G. Mouchaham, D.S. Sholl, R. Thyagarajan, D. Siderius, R.Q. Snurr, R.B. Goncalves, S. Telfer, S.J. Lee, V.P. Ting, J.L. Rowlandson, T. Uemura, T. Iiyuka, M.A. van der Veen, D. Rega, V. Van Speybroeck, S.M.J. Rogge, A. Lamaire, K.S. Walton, L.W. Bingel, S. Wuttke, J. Andreo, O. Yaghi, B. Zhang, C.T. Yavuz, T.S. Nguyen, F. Zamora, C. Montoro, H. Zhou, A. Kirchon, D. Fairen-Jimenez, How Reproducible are Surface Areas Calculated from the BET Equation?, Advanced Materials 34 (2022) 2201502. https://doi.org/10.1002/adma.202201502.
[35] J. Cejka, H. Bekkum van, A. Corma, F. Schuth, Introduction to zeolite science and practice, 3rd revised edition, 3rd ed.,, Elsevier, 2009.
[36] A. Galarneau, F. Villemot, J. Rodriguez, F. Fajula, B. Coasne, Validity of the t-plot method to assess microporosity in hierarchical micro/mesoporous materials, Langmuir 30 (2014) 13266–13274, https://doi.org/10.1021/la5026679.
[37] A. Galarneau, D. Mehlhorn, F. Guenneau, B. Coasne, F. Villemot, D. Minoux, C. Aquino, J.P. Dath, Specific surface area determination for microporous/mesoporous materials: the case of mesoporous FAU-Y zeolites, Langmuir 34 (2018) 14134–14142, https://doi.org/10.1021/acs.langmuir.8b02144.
[38] Y. Wu, X. Ren, Y. Lu, J. Wang, Rapid synthesis of zeolite MCM-22 by acid-catalyzed hydrolysis of tetraethylorthosilicate, Mater. Lett. 62 (2008) 317–319, https://doi.org/10.1016/j.matlet.2007.05.026.
[39] J.M.R. Gallo, C. Bisio, G. Gatti, L. Marchese, H.O. Pastore, Physicochemical characterization and surface acid properties of mesoporous [Al]-SBA-15 obtained by direct synthesis, Langmuir 26 (2010) 5791–5800, https://doi.org/10.1021/la903661q.
[40] V. Zholobenko, C. Freitas, M. Jendrlin, P. Bazin, A. Travert, F. Thibault-Starzyk, Probing the acid sites of zeolites with pyridine: quantitative AGIR measurements of the molar absorption coefficients, J. Catal. 385 (2020) 52–60, https://doi.org/10.1016/j.jcat.2020.03.003.
[41] E.J.M. Hensen, D.G. Poduval, V. Degirmenci, D.A.J.M. Ligthart, W. Chen, F. Maugé, M.S. Rigutto, J.A.R. Van Veen, Acidity characterization of amorphous silica-alumina, J. Phys. Chem. C 116 (2012) 21416–21429, https://doi.org/10.1021/jp309182f.
[42] D.J. Morgan, Resolving ruthenium: XPS studies of common ruthenium materials, surface, and Interface, Analysis 47 (2015) 1072–1079, https://doi.org/10.1002/sia.5852.
[43] J. Balcerzak, W. Redzynia, J. Tyczkowski, In-situ XPS analysis of oxidized and reduced plasma deposited ruthenium-based thin catalytic films, Appl. Surf. Sci. 426 (2017) 852–855, https://doi.org/10.1016/j.apsusc.2017.07.248.
[44] P. Schmidt-Winkel, W.W. Lukens, D. Zhao, P. Yang, B.F. Chmelka, G.D. Stucky, Mesocellular siliceous foams with uniformly sized cells and windows, J. Am. Chem. Soc. 121 (1999) 254–255, https://doi.org/10.1021/ja983218i.
[45] Z. Kowalczyk, S. Jodzis, W. Raróg, J. Zieliński, J. Pielaszek, A. Presz, Carbon-supported ruthenium catalyst for the synthesis of ammonia the effect of the carbon support and barium promoter on the performance, Appl. Catal. A Gen. 184 (1999) 95–102, https://doi.org/10.1016/S0926-860X(99)00090-3.
[46] M. Thommes, K. Kaneko, A.V. Neimark, J.P. Olivier, F. Rodriguez-Reinoso, J. Rouquerol, K.S.W. Sing, Physisorption of gases, with special reference to the evaluation of surface area and pore size distribution (IUPAC technical report), Pure Appl. Chem. 87 (2015) 1051–1069, https://doi.org/10.1515/pac-2014-1117.
[47] X. Wang, G. Lan, H. Liu, Y. Zhu, Y. Li, Effect of acidity and ruthenium species on catalytic performance of ruthenium catalysts for acetylene hydrochlorination, catal, Sci. Technol. 8 (2018) 6143–6149, https://doi.org/10.1039/c8cy01677a.
[48] J. Zhang, C. Li, H. Yuan, Y. Chen, Enhancement of aromatics production via cellulose fast pyrolysis over ru modified hierarchical zeolites, renew, Energy 184 (2022) 280–290, https://doi.org/10.1016/j.renene.2021.11.103.
[49] S. Scirè, R. Fiorenza, A. Gulino, A. Cristaldi, P.M. Riccobene, Selective oxidation of CO in H2-rich stream over ZSM5 zeolites supported ru catalysts: an investigation on the role of the support and the ru particle size, Appl. Catal. A 520 (2016) 82–91, https://doi.org/10.1016/J.APCATA.2016.04.011.
[50] T. Komanoya, H. Kobayashi, K. Hara, W.J. Chun, A. Fukuoka, Catalysis and characterization of carbon-supported ruthenium for cellulose hydrolysis, Appl. Catal. A 407 (2011) 188–194, https://doi.org/10.1016/j.apcata.2011.08.039.
[51] X. Ren, M. Guo, H. Li, C. Li, L. Yu, J. Liu, Q. Yang, Microenvironment engineering of ruthenium nanoparticles incorporated into silica nanoreactors for enhanced hydrogenations, Angewandte Chemie - International Edition 58 (2019) 14483–14488, https://doi.org/10.1002/anie.201908602.
[52] J. Yang, Y. He, J. He, Y. Liu, H. Geng, S. Chen, L. Lin, M. Liu, T. Chen, Q. Jiang, B. M. Weckhuysen, W. Luo, Z. Wu, Enhanced catalytic performance through in situ encapsulation of ultrafine ru clusters within a high-aluminum zeolite, ACS Catal. 12 (2022) 1847–1856, https://doi.org/10.1021/acscatal.1c05012.
[53] A. Aho, S. Roggan, K. Eränen, T. Salmi, D.Y. Murzin, Continuous hydrogenation of glucose with ruthenium on carbon nanotube catalysts, catal, Sci. Technol. 5 (2015) 953–959, https://doi.org/10.1039/c4cy01088d.
[54] G. Araujo-Barahona, K. Eränen, J.P. Oña, D. Murzin, J. García-Serna, T. Salmi, Solid foam Ru/C catalysts for sugar hydrogenation to sugar alcohols-preparation, characterization, activity, and selectivity, Ind. Eng. Chem. Res. 61 (2022) 2734–2747, https://doi.org/10.1021/ACS.IECR.1C04501.
[55] P.O.J. Koopman, A.P.G. Kieboom, H. Van Bekkum, Induction effects in liquid phase hydrogenation catalyzed by ruthenium on carbon, Colloids Surf. 3 (1981) 1–12, https://doi.org/10.1016/0166-6622(81)80030-3.
[56] I.L. Simakova, Y.S. Demidova, E.V. Murzina, A. Aho, D.Y. Murzin, Structure sensitivity in catalytic hydrogenation of galactose and arabinose over ru/c catalysts, Catal Letters 146 (2016) 1291–1299, https://doi.org/10.1007/s10562-016-1752-3.
[57] A. Aho, S. Roggan, O.A. Simakova, T. Salmi, D.Y. Murzin, Structure sensitivity in catalytic hydrogenation of glucose over ruthenium, Catal. Today 241 (2015) 195–199, https://doi.org/10.1016/J.CATTOD.2013.12.031.
[58] G. Araujo-Barahona, A. Goicoechea-Torres, K. Eränen, R.-M. Latonen, T. Tirri, A. Smeds, D. Murzin, J. García-Serna, T. Salmi, Kinetic studies of solid foam catalysts for the production of sugar alcohols: xylitol from biomass resources, Chem. Eng. Sci. (2023) 119130, https://doi.org/10.1016/J.CES.2023.119130.

[59] V.A. Sifontes Herrera, D.E. Rivero Mendoza, A.R. Leino, J.P. Mikkola, A. Zolotukhin, K. Eränen, T. Salmi, Sugar hydrogenation in continuous reactors: from catalyst particles towards structured catalysts, Chem. Eng. Process. - Process Intesif. 109 (2016) 1–10, https://doi.org/10.1016/J.CEP.2016.07.007.
[60] B. Tong, Z.C. Tan, Q. Shi, Y.S. Li, D.T. Yue, S.X. Wang, Thermodynamic investigation of several natural polyols (I): heat capacities and thermodynamic properties of xylitol, Thermochim Acta 457 (2007) 20–26, https://doi.org/10.1016/j.tca.2007.02.022.
[61] G. Araujo Barahona, K. Eränen, D. Murzin, J. García Serna, T. Salmi, Reaction mechanism and intrinsic kinetics of sugar hydrogenation to sugar alcohols on solid foam Ru/C catalysts – from arabinose and galactose to arabitol and galactitol, Chem Eng Sci 254 (2022) 117627, https://doi.org/10.1016/J.CES.2022.117627.
[62] A. Najarnezhadmashhadi, J. Wärnå, K. Eränen, H.L. Trajano, D. Murzin, T. Salmi, Modelling of kinetics, mass transfer and flow pattern on open foam structures in tubular reactors: hydrogenation of arabinose and galactose on ruthenium catalyst, Chem. Eng. Sci. 233 (2021) 116385, https://doi.org/10.1016/J.CES.2020.116385.
[63] E. Toukoniitty, J. Wärnå, D.Y. Murzin, T. Salmi, Modelling of transient kinetics in catalytic three-phase reactors: enantioselective hydrogenation, Chem. Eng. Sci. 65 (2010) 1076–1087, https://doi.org/10.1016/j.ces.2009.09.062.
[64] E. Toukoniitty, B. Ševčíková, P. Mäki-Arvela, J. Wärnå, T. Salmi, D.Y. Murzin, Kinetics and modeling of 1-phenyl-1,2-propanedione hydrogenation, J. Catal. 213 (2003) 7–16, https://doi.org/10.1016/S0021-9517(02)00025-8.
[65] D.Y. Murzin, V.Y. Konyukhov, M.I. Temkin, Liquid-phase hydrogenation of cyclohexene on platinum and palladium catalysts, Kinet. Catal. 29 (1988) 1–7.
[66] M.I. Temkin, D.Y. Murzin, N.V. Kul'kova, Kinetics and mechanism of liquid-phase hydrogenation, Dokl.an USSR 303 (1988) 555–561.